UNIVERSITÀ DEGLI STUDI DI PADOVA

Dipartimento di Fisica e Astronomia "Galileo Galilei"

Master Degree in Astrophysics and Cosmology

Final Dissertation

A Decade of Cometary Spectroscopy
from the Asiago 1.22m Telescope

Supervisor: Candidate:

Prof. Fiorangela LA FORGIA   **Alessandra MURA**

Co-supervisor:

Dr. Paolo OCHNER

Academic Year 2022-2023

Contents

5   Conclusions   **43**

Appendix A   Asiago Atlas of Comets - Complete Spectral Dataset

Abstract

This thesis presents an insight into comet spectroscopy conducted at the Asiago Astrophysical Observatory over ten years.

The seeds of this work were laid by my involvement in the direct observation with the 1.22m Galileo telescope of three specific comets (C/2023 E1, C/2023 H2, 12P) during their voyage towards the perihelion.
Spectra from these comets were reduced using standard IRAF procedures and a Python code was developed to calculate the production rate of the most prominent band in cometary optical spectra, the CN violet band system at 3880 Å, within the framework of a simplified Haser model. This analysis was extended to the broader sample of the Asiago Atlas of Comets project, adapting the procedure to the data available. The results have been validated through a comparison with existing literature, demonstrating a strong agreement.

The study unveiled a correlation between dynamical comet types and their distribution on the production rate vs. heliocentric distance plane, indicating that 'new' dynamical types tend to show higher values of Q(CN), while comets captured by Neptune or Jupiter have lower values.

A detailed follow-up analysis of specific comets revealed noteworthy patterns. Comet C/2023 E1 displayed an asymmetry in production rate concerning perihelion, with the maximum rate occurring post-perihelion. Similarly, comet C/2023 H2 exhibited this asymmetry, with nuanced variations in rates before and after perihelion. Comet 12P showed distinct peaks in its production rate corresponding to recurring outburst events, providing valuable insights into the dynamic nature of cometary behaviour.

Chapter 1

Introduction

1.1 Comets

Comets are minor bodies of the Solar System and they are thought to be leftovers from planetary formation. Whether it is still debated if cometary nuclei formed directly in these regions (van Dishoeck et al., 2014) or moved there as a consequence of the solar system's gaseous giants (Jupiter and Saturn) migration (Dones et al., 2004), they are in any case fundamental tracers of the thermal and compositional history of the Solar System (Ceccarelli et al., 2022).

Their composition has been explored with spectroscopy, but the real revolution was made by the two close encounter missions, for example, Deep Impact, which in 2005 released an impactor on comet 9P Tempel. Nine years later Rosetta mission became the first ever spacecraft to perform a physical follow-up of a comet, joining its orbit towards the perihelion. It was also the only case of comet landing, achieved by the little module Philae.
The results of these missions were a deeper understanding of cometary morphology and composition. Cometary nuclei were proven to be mostly composed of refractory material and volatile ices (Fig. 1.1), which are thought to be the most pristine material remaining from the original pre-solar nebula (Mumma and Charnley, 2011). The composition of these ices is for $\sim 80\%$ water ices, followed by CO_2, CO, CH_3OH, CH_4, H_2S and NH_3 (Bockelée-Morvan and Biver, 2017). Furthermore, cometary nuclei have been discovered porous and low-density. It is not rare to observe a bilobate shape, possibly implying they underwent low-speed impacts (Fornasier et al., 2015), (Sierks et al., 2015), (Massironi et al., 2015).

It is commonly recognized that the Kuiper belt and the Oort cloud are the reservoirs of cometary nuclei, where they lay in their dormant state. Gravitational interactions with nearby stars or giant molecular clouds can disturb the orbits of objects in the Oort Cloud, sending some of them inward toward the solar system (Hills, 1981). The mechanisms that bring Kuiper Belt comets into the inner solar system are somewhat different from those affecting Oort Cloud comets. In this sense, the influence of Neptune plays a crucial role. Cometary nuclei orbits may be altered by Neptune's gravitational influence, or they may enter into resonant orbits with the giant planet. Subsequently, further interactions with Jupiter or Saturn may cause their orbit to be further reduced.

Depending on which kind of orbit they are inserted into, they are divided into two main categories. Long-period comets (period over 200 years) are further distinguished in "Returning" if their eccentricity is below 1 and "Dynamically New" if they have eccentricity ≥ 1 and semimajor-axis > 10000 AU. Short-period comets (period < 200 years) can belong to the Jupiter Family group if their period is < 20 years, while they are defined as "Halley Type" if the period is over 20 years

(but still below 200 years).

On its way to reach the perihelion, the nucleus is heated by the Sun's radiation, which triggers the sublimation process of the ices here enclosed. At this point, the comet is properly defined as active, and the coma and tails start to form and become visible to telescopes and, for the most brilliant ones, even the naked eye. In the visible regime, the sublimation of volatiles like CN, C_2 and C_3, begin at larger distances, 2-3 Astronomical Units (AU) and the nucleus exhausts their reservoirs leaving less to sublime for further solar passages. Actually, cometary activity has been observed even up to ~ 26 AU, but only for species called "super volatiles", like CO and CO_2, detectable in the near-infrared regime. This is the case of comets C/2010 U3 Boattini (active at 25.8 AU) (Hui et al., 2019), C/2017 K2 (23.75 AU), here treated, (Meech et al., 2017) and C/2014 UN271 Bernardinelli-Bernstein (23.8 AU) (Farnham et al., 2021).

Sublimed gaseous components are subject to interaction with the highly energetic charged particles emitted by the Sun, which causes their ionization. Once charged, the comet's radicals are forced to follow the Sun's magnetic field lines: an ion tail forms, which points straightly in the anti-solar direction. Along with the sublimation process, small chunks of refractory material are also ejected from the nucleus. The solar radiation pressure and the inertia of the nucleus motion along the orbit are now acting on the dust. The combination of these two components extends the dust tail in the anti-solar direction, just like the ion tail, but with a curvature given by the orbital motion. For this reason, when the comet is at the perihelion, the different orientations of the two tails reach its maximum.
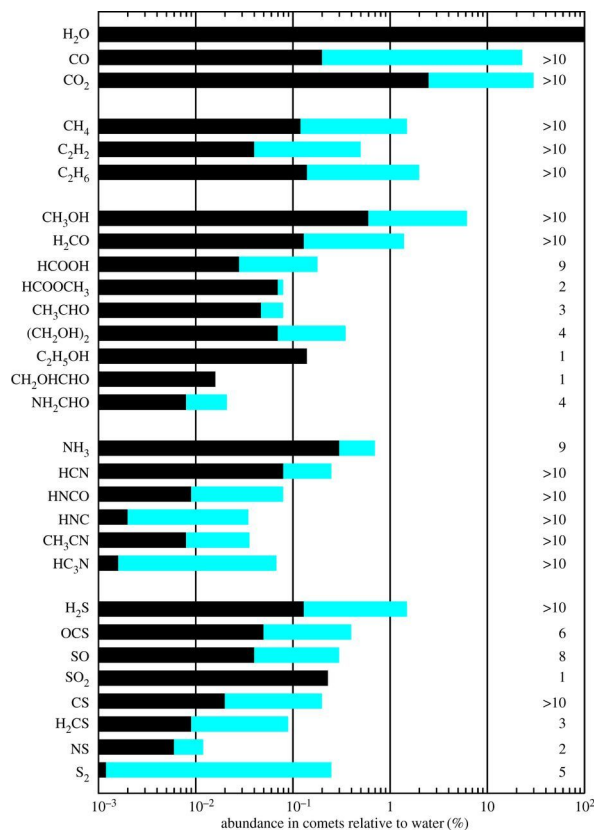

Figure 1.1: *Abundances of molecules detected with spectroscopy relative to water. Bars in blue indicate the full range of measured quantities in comets. Source: Bockelée-Morvan and Biver (2017).*

1.2 Cometary Surveys

The 1970s and 1980s witnessed the birth of the first photometric and spectroscopic surveys aimed at evaluating the production rates of the chemical species observed in comets.

A'Hearn in 1970 started one of the most extensive narrow-band photometric surveys from the Lowell Observatory. Early results were published in A'Hearn and Millis (1980), and discussed in A'Hearn et al. (1995). They obtained optocenter-centered aperture photometry thanks to a set of special filters with large apertures (>30") designed to isolate the cometary molecular emissions. Newburn and Spinrad (1984) and Cochran (1987) followed their lead with two spectroscopic surveys, respectively from Lick and McDonald Observatory with the very purpose of determining molecular production rates. Newburn and Spinrad (1984) had a 25-comet sample, while Cochran (1987) had 17. Both of these surveys obtained spectra from an image dissector scanner (IDS). The IDS datasets generally have spectra obtained with small apertures (4-7") in the optocenter and at various positions within the coma.

More recently, Fink (2009) presented a spectroscopic observations of 92 comets. Fink (2009) notes that Newburn and Spinrad (1984) and Cochran et al. (1992) method of IDS multiple aperture produces data with a higher scatter with respect to his long-slit CCD data. This complicates considerably the task of discerning trends in the production rate ratios. Later on, Langland-Shula and Smith (2011) analysed the spectra of 26 comets, and Cochran et al. (2012) have reported measurements of abundance ratios from observations of 130 comets made at the McDonald observatory over 30 years. All of these are long-slit spectroscopy-based surveys.

The analysis of such a gathering of data is the way to answer some long-dated questions on these celestial bodies: are comets generally equivalent in their composition or do there exist composition classes? May these classes be indicative of their region of origin? Or if a constancy in the composition exists, do large outliers emerge? The subsequent years of data analysis have laid the foundations for the current knowledge on cometary spectral variety.

The data gathered and analyzed from surveys in the 1980s gave rise to many speculations about the information that can be extracted from a cometary spectrum.

The first point to be explored was if there were noticeable differences in the cometary spectra (thus leading to a new classification) or if all comets show the same features. The optical spectra are observed to show generally similar components. The only variables are the amount of continuum, related to dust activity, and the emission band strengths, relative to the molecular production rates. By measuring the relative abundance between these species, attempts to classify comets by their spectra can be made. According to (Cochran et al., 2012), the main differentiation is between a "typical" spectrum and one showing depletion in carbon-chain molecules C_2 and C_3. A'Hearn et al. (1995) gave as a definition for depletion $\log(Q(C_2)/Q(CN)) < -0.18$. Cochran et al. (2012) instead uses the definition $\log[Q(C_2)/Q(CN)] \leq 0.02$ and $\log[Q(C_3)/Q(CN)] \leq 0.86$.

Fink (2009) divides spectra in his sample into four taxonomic groups: typical comets; comets with typical ratios of C_2, NH_2 and CN exhibiting typical ratios with respect to water; Tempel 1 type, with low C_2 amount but normal in NH_2; Giacobini-Zinner type showing depletion in both C_2 and NH_2; then an unusual object in the sample, Yanaka (1988r) which has no evidence of CN or C_2 emissions, but shows a typical amount of NH_2.

A'Hearn et al. (1995) found that comets from the Kuiper belt appear to be systematically depleted in the carbon-chain molecules generating C_2 and C_3 in the spectra. Furthermore, they suggest the observed depletion of the carbon-chain in Jupiter family comets could be explained as unevenness in the original solar nebula. Cochran et al. (1992) pointed out that the production rate ratios
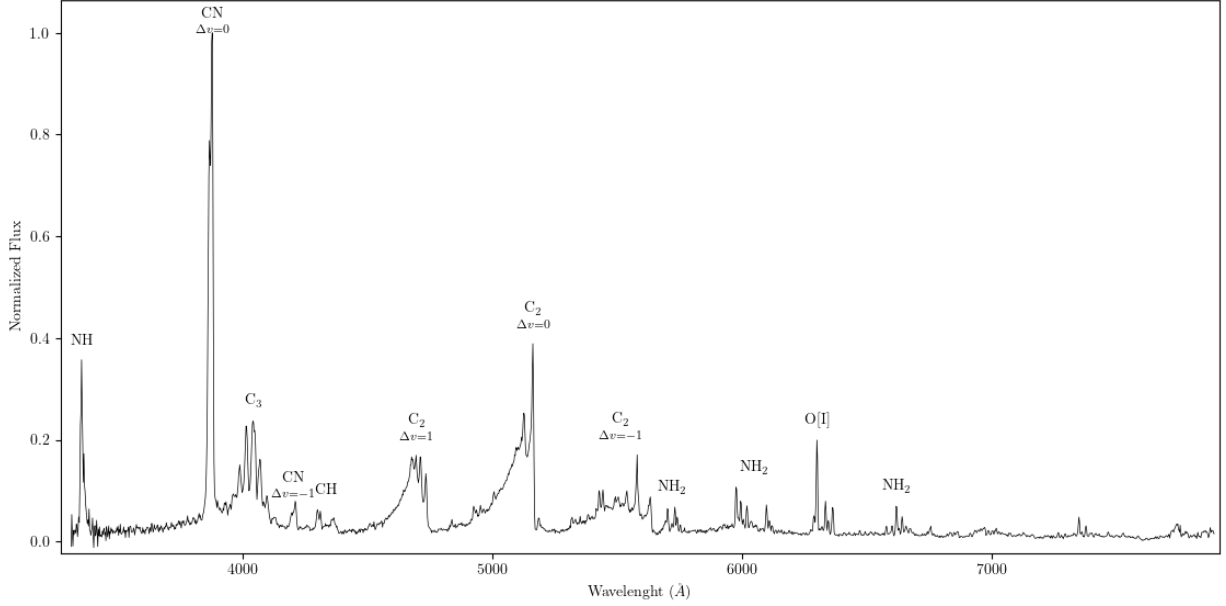
Figure 1.2: *An example of a typical cometary spectrum. All main emission bands are visible. The cometary spectrum is divided by the solar analog Land 107-684 to remove the dust reflectance spectrum. C/2023 E1 ATLAS, 2023-06-25, 300 lines/mm grating, 150 µm slit. 1.22-m Galileo telescope, Asiago Observatory.*

of various molecules remained constant over various ranges of heliocentric distance. Gilbert et al. (2010) found a linear correlation between production rates of C_2 ($\Delta \nu = 0$), C_2 ($\Delta \nu = 1$) and C_3 with respect to CN. A hint of this correlation was already noted by Cochran et al. (1992) while analysing the first results of her survey at the McDonald observatory. She also found no evidence of a correlation between the production rate ratios and heliocentric distance.

1.3 Cometary Spectra

The chemical environment of the coma is mostly explored by observing its emission spectra, which gives also glimpses of the nucleus composition. These kinds of studies allow the researchers to inquire about the nuclei formation within the protoplanetary disk, but also its thermal processing history(Ceccarelli et al., 2022). The majority of the species observed at optical and UV wavelengths are radicals, atoms, and ions. They do not sublimate directly from the nucleus but are produced in the coma through the photodissociation of parent molecules and chemical reactions (Bockelée-Morvan et al., 2004). For example, the most common reaction is the photodissociation of water molecules into hydroxyl and hydrogen radicals:

$$H_2O + h\nu \longrightarrow H + OH \tag{1.1}$$
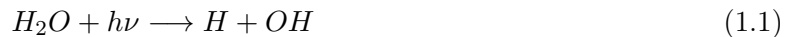
where h is the Planck constant and ν is the frequency of the solar photon. A cometary spectrum is characterized by two components: a reddened solar spectrum reflected by the dust, and an emission spectrum given by the gases.

Emission lines are produced through collisional or radiative excitation processes. Since cometary comae are low-density environments, collisions are generally neglected. Radiative processes are the most common and they produce transitions between electronic, rotational and vibrational energy levels. Electronic transitions appear in the ultraviolet range and they are rare to observe, as the

7

interaction with the Sun's UV radiation is more likely to just split the molecule into its radicals. Rotational and vibrational transitions are seen in the infrared and microwave range and can be observed through resonance fluorescence, which is the process of absorption followed by spontaneous re-emission.

The kind of emission lines or bands detectable in the spectrum varies with the spectral range analyzed. In the visible range (3000-8000 Å) dominates the CN ($B^2\Sigma^+ - X^2\Sigma^+$) violet system, with its $\Delta\nu = 0$ band near 3880 Å (Section 2.1.1) being one of the strongest spectral features in comets, almost always detectable (Feldman et al., 2004). Also, this line shows a strong Swing effect (brief explanation in Section 2.1.1). Right near this peak is found the C_3 ($A^1\Pi_u, -X^1\Sigma_g^+$) band at 3920-4100 Å. Finally the C_2 Swan ($d^3\Pi_g, -a^3\Pi_u$) bands: $\Delta\nu = 1$ at 4500 - 4745 Å, $\Delta\nu = 0$ at 5000 - 5174 Å and $\Delta\nu = -1$ at 5410 - 5640 Å.
Other identified features in a visible spectrum are lines of NH_2, which are various and scattered along the spectrum (Cochran and Cochran, 2002), CH (4300-12 Å), ion H_2O^+ and, only for heliocentric distances r≤1, [OI] ^{1}D lines (5577, 6300, 6364 Å) and the sodium doublet (5890, 5896 Å). An example of a comet observed from Asiago Observatory showing all the main bands in an optical spectrum is C/2023 E1 ATLAS, which spectrum is shown in Fig. 1.2.
On the basis of the relative band strength, usually, C_3/CN or C_2/CN, cometary spectra have been classified into two macro-categories: "typical" and "depleted" (Cochran et al., 2012), where depleted refers to a depletion observed in the carbon-chain molecular bands (more details in Section 1.2).

1.4 This Work: the Production Rate of CN Violet System of the Asiago Observatory Comets

The purpose of this thesis is to bring to light a considerable work of data gathering done in the last ten years at the 1.22 Galileo telescope of the Asiago Observatory, which includes more than 130 spectra of 38 comets. It is fundamental to focus on the analysis of this existing database, to widen the current knowledge in the variety of cometary spectra. We claim the analysis of the Asiago comets could make a significant contribution to past survey results and renew their actual knowledge.

Being the CN violet system, with its (0-0) transition one of the most intense emission bands in the visible spectra of comets, this work is focused on investigating the CN production rate for the whole Asiago sample, in the framework of a simple Haser model (Section 2.2). The procedure has been validated by doing a comparison with the results obtained by other authors (Section 4.1.1). A subset of data is formed by comets that I followed during my thesis internship. I contributed to this sample by taking part in the observations and reducing the data using IRAF software (Section 3.5). These comets are the Halley Type C/2023 E1 the Returning C/2023 H2 and the peculiar outbursting Jupiter Family comet 12P Pons-Brooks. This subset was my starting base for learning the standard reduction procedures and adapting them for cometary data. It also allowed me to develop the code for computing the CN production rate. The knowledge gained from studying these comets was then applied to the whole sample, composed of past data (covering a period from 2013 to 2022) already reduced using the IRAF-based pipeline developed for analyzing 1.22m telescope images.

This thesis is organized as follows: firstly, an overview of the Haser model is presented along with its details for usage. Secondly, the data reduction procedure is focused on, from the first steps of the calibration (bias subtraction, flat-fielding,) up to the flux calibration. Thirdly, the analysis of the resulting fluxes and the method used to compute the production rates is discussed. Finally,

the results are compared with the literature and an overall summary is provided.

Chapter 2

Theoretical Framework

This chapter provides the theoretical background knowledge necessary to understand the analysis work illustrated in the following chapters. Firstly, it discusses in detail the nature of the CN violet system, its production process in the cometary coma and the underlying mechanisms that affect its behaviour. Subsequently, an overview of the Haser model is presented, which is used to calculate production rates, and its application in this study is explained.

2.1 The CN violet system

2.1.1 The CN radical in comets

The bands of the CN violet system (B-X, $\Delta\nu = 0$) were identified by William Huggins in the first photographic spectrum of comet Tebbutt, the Great Comet of 1881. It was clear from the beginning this was one of the strongest cometary spectral features in the optical regime and it would have become one of the most diffused and studied features in cometary optical spectra.

The CN $\Delta\nu = 0$ band appears in a low-medium resolution spectrum as a two-peaked profile, as enlarged in Fig. 2.1. This shape is the result of the convolution of roto-vibrational transitions from the two lowest electronic levels, $X^2\Sigma^+$ and $B^2\Sigma^+$ represented in high spectral resolution in Fig. 2.2. The third low energy level, $A^2\Pi_i$ produces instead the red CN system, (7908-8067 Å), due to A-X transitions.

When a molecule is exposed to solar radiation, its electrons in the ground state get excited to a higher energy level. However, these excited states are unstable and the molecule subsequently releases a photon:

$$CN(X^2\Sigma) + h\nu_{ex} \longrightarrow CN(B^2\Sigma, \nu' = 0, 1, 2...) + h\nu_{em} \tag{2.1}$$
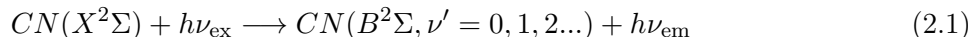
where ν_{ex} is the exciting photon frequency, and ν_{em} is the emitted photon frequency, h is the Planck constant. This is the definition of the fluorescence process and it is most likely what happens to radicals in the coma of comets.

Fluorescent equilibrium models (Arpigny, 1964), Ishii and Tamura (1979) manage in fact to reproduce quite well the CN spectrum observed in comets and in particular its observed strong dependence on the heliocentric radial velocity of the comet. This is known as the Swing effect (Swings, 1941). Swing noticed the band shape was influenced to a high degree by the presence or absence of the Fraunhofer absorption lines of the solar spectrum at the same wavelength of the molecular absorptions. In this sense, the heliocentric radial velocity of the comet plays an important role, as the Doppler-shifted solar radiation may or may not have the Fraunhofer lines at the same wavelength of the molecular absorption. This Swing effect modifies both the intensity distribution among the rotational lines and the total luminosity of the band. It is known how all diatomic
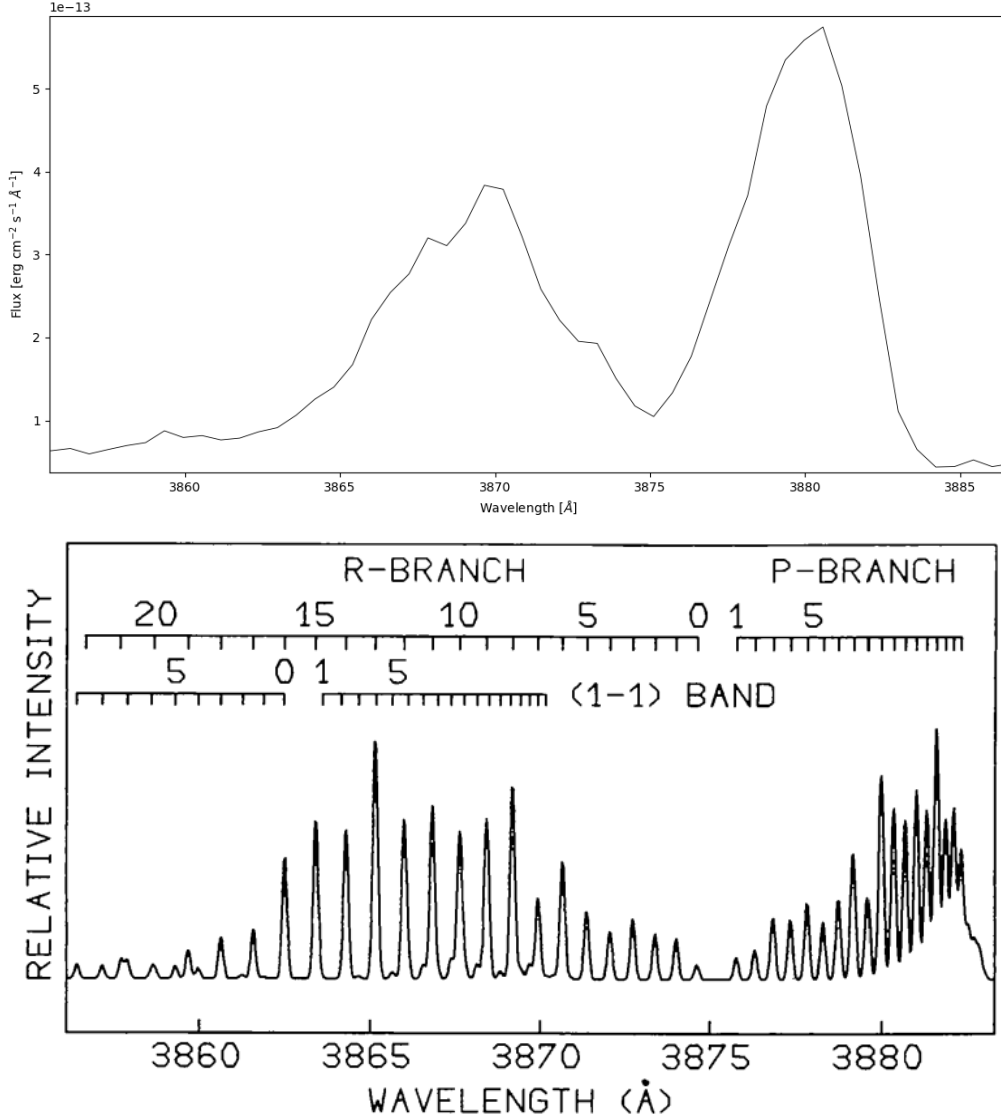
Figure 2.1: *Spectrum of the CN $\Delta\nu = 0$ band of comet 67P made with the 1200 lines/mm grating of the 1.22m Galileo telescope (upper) compared with a high-resolution synthetic spectrum, from Zucconi and Festou (1985) (lower). In the lower image R and P branch transitions are labelled both for (0-0) and (1-1) sequences.*

molecules observed on comets show the Swing effect with different intensities. However, the CN violet band seems more subject to these variations.

By solving the equation imposing the equilibrium between emission and absorption one may find the fluorescence equilibrium solution thanks to which one can know the partition of the electrons in every energetic level, the level population density n_i. By knowing n_i of the single transition composting the band, the excitation rate (or g-factor) of the fluorescence process can be computed as:

$$g_{line} = n_i A_{ij} \tag{2.2}$$

where g_{line} is the excitation rate of an emission process from the upper level i to the lower level j, n_i is the population of level i and A_{ij} is the Einstein factor associated to the transition from i
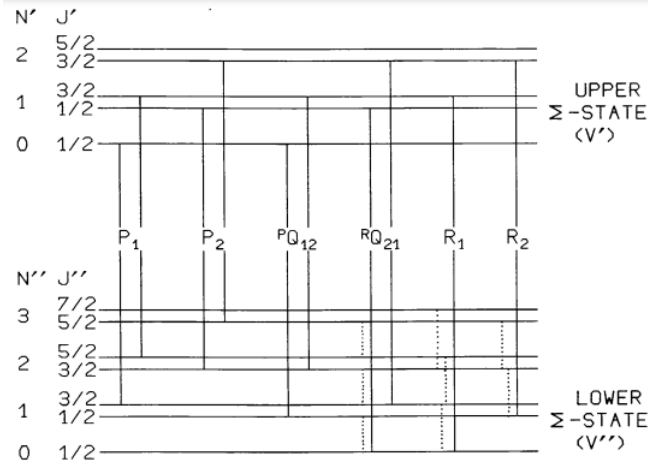
Fig. 1. Schematic diagram showing the first allowed transitions between two vibrational sigma-state sub-levels. Dotted lines represent pure rotational transitions. Levels are labelled by their quantum numbers N and J (Note that there is no Q-branch).

Pure rotational and vibrational transitions in the upper state can be neglected because of the very fast decay of this state through an electronic transition toward the lower electronic state

Figure 2.2: *Source: Zucconi and Festou (1985)*

to j, which expresses the probability of the transition in terms of number of processes per seconds. The fluorescence efficiency of the whole band is simply the summation of the g-factors of individual lines. This quantity is of fundamental importance for the computation of the production rate, and it is discussed ahead (Section 2.2).

Figures 8 and 9 from Zucconi and Festou (1985) provide a powerful visualization how the Swing effect makes these bands' excitation rates change dramatically with the heliocentric radial velocity of the comet, leading to visible changes in the CN profile shape. The details of this effect are clearly depicted in Fig. 2.3.

While fluorescence is a widely accepted theory for the CN emission spectrum, it is still not clear what brings the CN in cometary coma in the first place. The main process related to CN radical production is the photodissociation of HCN (Myer and Nicholls, 1970):

$$HCN + h\nu \longrightarrow H + CN(X^2\Sigma, \nu = 0), \tag{2.3}$$
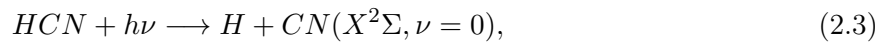
However, it is not clear if the dissociation of HCN is actually the main cause of the presence of the CN radical. Different studies found out the abundance of HCN and even C_2H_2 were not enough to explain the observed abundance of CN (De Almeida et al., 1989), suggesting this may be a possible production source, but not the only one. Another possibility is that CN is part of a distributed source in the coma, probably coming from photo and thermal degradation of dust (Cottin and Fray, 2008).
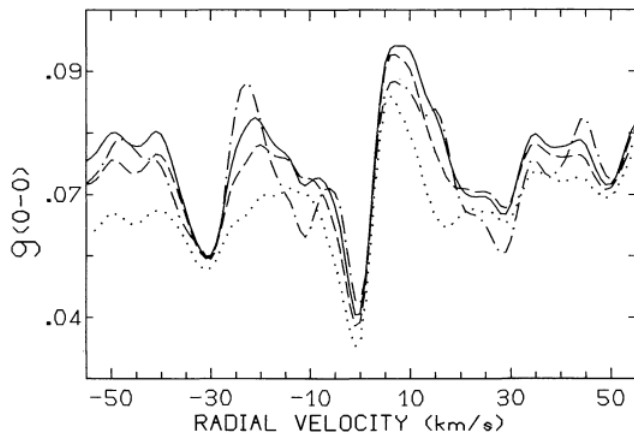
Fig. 7. Excitation rates (s^{-1}) of the violet (0–0) band of CN for $r = 0.5$ a.u. (dotted line), 0.75 a.u. (dashed line), 1 a.u. (full line) and 2 a.u. (dashed dotted line). The Swings effect is responsible for a tremendous apparent size increase of the CN cloud when the comet has passed through its perihelion. All values have been multiplied by r^2
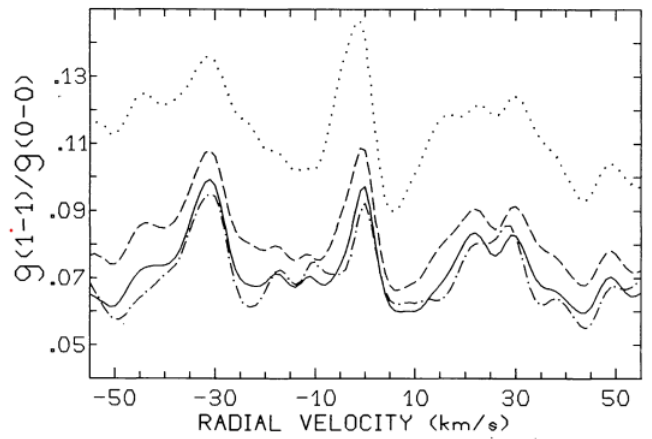
Fig. 8. Variation of the ratio of the excitation rates of the (1–1) to the (0–0) violet band when the radial velocity varies between -55 and $+55$ km s^{-1} for $r = 0.5$ a.u. (dotted line), 0.75 a.u. (dashed line), 1 a.u. (full line) and 2 a.u. (dashed dotted line). The (1–1) band must clearly be studied at small heliocentric distances or near $\dot{r} \sim 30$ km s^{-1} or $\dot{r} \sim 0$ km s^{-1}

Figure 2.3: *Source: Zucconi and Festou (1985).*

2.2 The Haser Model

The Haser model, developed by Alexander Haser in 1957 (Haser, 1957), is a theoretical framework that provides a mathematical way to describe the distribution followed by the molecules in the environment of a cometary coma. This model is based on a simplification of the actual processes occurring in a real coma. In particular, these assumptions are:

- The comet is assumed to have a spherically symmetric nucleus and coma;

- The parent molecules are uniformly emitted from the nucleus surface with a constant outflow velocity and then disrupted through photolysis into daughter species, following the law:

$$n = n_0 e^{-\frac{t}{\tau_0}}, \tag{2.4}$$

  where n_0 is the number of molecules at time $t = 0$ and τ_0 the average lifetime of a molecule subject to the solar radiation field;

- The process responsible for the production on the emission lines is fluorescence resonance triggered by interaction with solar radiation;

- The molecular density near the nucleus does not vary;

- Collisional processes are neglected.

Haser assumes the only mechanism producing the observed species (called "daughter" molecules) is the photodissociation of a "parent" molecule. In this way, every daughter is produced by a unique progenitor and no further dissociations are considered. For example, in the case of CN, it is assumed that the only progenitor is the HCN molecule. The characteristics of daughter and parent species are described by their respective "scale length". These l_p and l_d appear in the mathematical expression of the model (Eq. 2.5) as two parameters, whose value has to be found as a result of the best fit with the observations. These two parameters should represent the single-step photodissociation process from parent to daughter. In reality, the production of observed radicals is more complex than that. For example, an observed daughter species may have different progenitors. Or the final daughter may not be the result of a single photodissociation, but of a chain of said process. This is the reason why the Haser scale length cannot be seen as physical lengths but rather as "effective" lengths.

The mathematical form of the model is given by:

$$n(\rho) = \frac{Q}{4\pi v \rho^2} \left(\frac{l_d}{l_p - l_d} \right) \left(e^{-\frac{\rho_n}{l_p}} - e^{-\frac{\rho_n}{l_d}} \right) \tag{2.5}$$

Where ρ is the nucleocentric distance Q is the molecular production rate, v is the outflow speed, ρ_n the reduced nucleocentric distance, which is ρ minus the nucleus radius, l_d and l_p daughter and parent scale length, which are given by the parent/daughter lifetime multiplied by the outflow velocity.

This formulation manages to reproduce quite well the observed trend in the gas distribution on a comet's coma. By fitting the model to the observed distribution of a certain molecule, it is possible to derive its production rate Q [mol s^{-1}]. Usually, there are two ways used by different authors of dealing with the outflow velocity: to assume it to 1 km s^{-1}, following (Fink and Hicks, 1996), or adopt the Delsemme formula, 0.85 $r^{-0.5}$, as Churyumov et al. (1990) or Cochran (1985). This leaves only Q, l_p and l_d as unknowns.
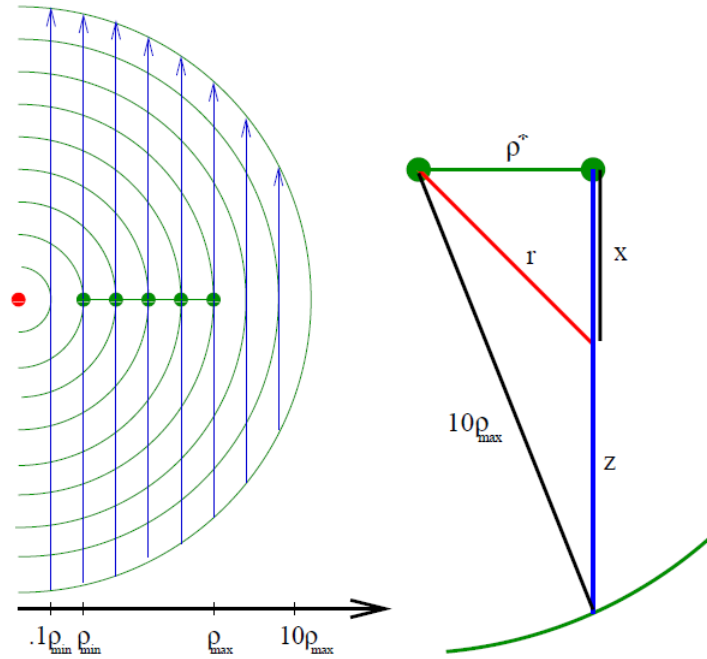
Figure 2.4: *Visualization of the line of sight integration of the Haser model. ρ^* (green dots) is the sky plane projected nucleocentric distance. The green lines are the lines of equal number density yielded by the model. The blue lines give the line of sight at every ρ^*. Source: Helbert (2003).*

Actually, the implementation of this model would consist of performing a three-parameter fit of Eq. 2.5 on the observed distribution of the gas in the coma. Cochran (1985) notices that the Haser model provides an overall good fit with the data, but only if a way of assuming at least one of these three parameters is found. Usually, the used approach is to leave Q as the only free parameter and assume the scale lengths, rather than the computationally complex three-parameter fit. To this purpose, various sets of scale lengths have been computed through the years. The main collections are A'Hearn (1982), Cochran (1985) A'Hearn et al. (1995) Cochran and Schleicher (1993) Randall et al. (1992) Cochran and Cochran (1990) Cochran et al. (1992) Fink et al. (1991). All recent publications refer to one of these sets, based on which fits better their observations. Conversely, when an author decides to compute its set of scale lengths if the one found in the literature does not produce satisfactory fits, they use a recursive method: firstly they perform the fit with a given set. This fit is used to have a first estimation of the production rate. Then fix Q and re-do the fit, this time to compute the best fit for the scale lengths. This procedure is performed until a minimum in the fit's standard deviation is reached.

Coming to the assumption of fluorescent resonance as the main transition of the radical, this is a more acceptable assumption, particularly for the CN band which is here analysed (Swings, 1941) (Arpigny, 1964), (Ishii and Tamura, 1979). This assumption enters the model with the presence of the fluorescence efficiency (g-factor). This parameter is a way of quantifying the luminosity of a molecule in the solar radiation field, and it is computed thanks to fluorescence equilibrium models (Section 2.1.1).

While the Haser model has proven to be a valuable tool, it is important to acknowledge its limitations. The assumed spherical symmetry may not hold true for all comets, and deviations from constant outflow velocities have been observed. Recent advancements involve incorporating additional complexity into the model, such as non-spherical distributions and variable outflow

velocities, to better capture the nuances of cometary comas. However, its vast usage is owed to its simplicity in terms of calculation and the general goodness of the observed gas distribution fit on an empirical basis. As noted by Cochran (1987), the Haser model, despite not being valid to give a physical representation of a comet's inside, is a good way to put all kinds of observations on the same plane, so it is a good way of comparing different data from a huge dataset or data coming from different datasets.

2.2.1 Approach to the Haser model

To obtain the CN production rate, we did not use the Haser model to fit the column density distribution along the long-slit aperture. This would have necessitated the flux-calibrated bidimensional spectrum to be available. Since the spectra were old and the availability was limited, a different approach is needed. To convert integrated fluxes to molecular production rate we refer to the work of (Fink and Hicks, 1996). The molecular production rate Q (mol s^{-1}) of a species produced by resonance fluorescence, as in the case of CN blue band, can be computed as follows:

$$Q = \frac{4\pi\Delta^2 \cdot v_{out}}{g \cdot l_d} \cdot Flux \cdot HC \tag{2.6}$$

Where Q (mol s^{-1}) is the molecular production rate, Δ (km) is the Geocentric distance, g (erg s^{-1} mol^{-1}) is the fluorescence efficiency (Schleicher, 2010), l_d (km) is the parent scale length, Flux (erg cm^{-2} s^{-1}) is the total integrated flux and HC is the Haser Correction. $4\pi\Delta^2$ is the radiation dilution factor. The components of this equation are based on several assumptions:

- The fluorescence efficiency g (erg s^{-1} mol^{-1}) is a way of quantifying the luminosity of a molecule in the solar radiation field and, consequently, it is linked to its production rate. By using this quantity it is assumed the violet CN band is produced by the fluorescence resonance process, a fact to date widely accepted (Swings, 1941) (Arpigny, 1964), (Ishii and Tamura, 1979). The g-factors are computed through fluorescent equilibrium models, providing CN molecule luminosity in the solar radiation field as a function of the comet heliocentric distance and velocity. The most recent tabulated values are given in Table 2 of Schleicher (2010), which were double-interpolated to obtain fluorescence efficiency values for the heliocentric distance and velocity of every comet. The g-factors used in the analysis are reported in Tab. 3.5.

- In the context of a simple Haser coma outflow model (Haser, 1957) the total number of emitting molecules in the coma is computable, even if the observations are bound by finite apertures. This is done by scaling the observed flux by a factor, the Haser Correction. The definition of HC is the inverse of the ratio of the number of emitting species within the aperture to the total number of emitting species if the aperture were infinite. The computation is done thanks to the software provided by Schleicher at the Lowell Observatory website[1]. This tool performs its routine using the set of scale lengths provided by Randall et al. (1992) (Tab. 3.5), properly scaled with the heliocentric distance (r$_h$) with a factor r_h^2.

- $4\pi\Delta^2$ is the radiation dilution factor, that describes the concentration of the radiation at a certain distance from the source.

- The outflow velocity is assumed to be v_{out}(km s^{-1}) = 1 on the base of the analysis conducted by Fink and Hicks (1996).

---

[1] https://asteroid.lowell.edu

Chapter 3

Methods

3.1 Procedure Summary

The procedure followed to obtain the final production rate of the CN molecule from the raw images is here summarized. The raw spectra collected at the telescope are bias- and dark-subtracted, flatfield-corrected and wavelength- and flux-calibrated using the standard IRAF procedure (Section 3.5). The bidimensional clean spectrum is extracted to have a monodimensional spectrum by selecting an aperture width, and then summing the flux over the slit width direction. The region containing the CN emission band is selected (3500-3920 Å). Herein, a double-gaussian function along with a linear function are fitted to measure the flux within the emission band and set the continuum level (Section 3.7). The flux integral over the band is taken and then converted to molecular production rate according to a simple Haser model, which assumptions and computation methods are described in Section 2.2).

3.2 Instrumentation

All the cometary spectra here analyzed are taken at the 1.22m Galileo telescope (DFA-Unipd[1]) in Asiago (Tab. 3.1).

The telescope Cassegrain focus is equipped with a Boller & Chievens spectrograph, designed by Perkin Elmer. The spectrograph long-slit aperture has a fixed length of 28 mm and a variable width, reaching a maximum aperture of 1 mm. The beam is collimated towards the grating location through an off-axis parabolic mirror with a focal length of 810 mm.

The set of available gratings guarantees a spectral coverage from 3300 Å to beyond 7800 Å with a dispersion reaching 0.6 Å/px. The dispersed light is focused on two combined cameras, the ANDOR iDus 440A Sensor E2V 42-10BU Back Illuminated CCD and the Dioptric Blue Galileo Camera. The CCD sensor has a matrix of 2048x512 pixels, each with a size of 13.5x13.5 μm, corresponding to an active image area of 27.6x6.9 mm and a resolution of 1"/px.

The slit has a reflective side, which allows the observer to visualize the telescope's focal plane during the acquisition of a spectrum. The guiding camera is an ANDOR iXon DV885 with EMCCD Technology, with an effective field of view of 8.2'x5.5' and a resolution of 0.68"/px.

There are five available hollow cathode comparison lamps for wavelength calibration, Fe-Ar, He-Fe-Ar, Hg-Ar, Ne and Hg-Ar-Ne. In Tab. 3.1 is resumed technical information about the telescope and its grating set.

---

[1]Dipartimento di Fisica e Astronomia, Università di Padova.

The Telescope		The Location	
Primary Diameter	1237 mm	Longitude	E11° 31' 35.138"
Secondary Diameter	1200 mm	Latitude	+45° 51' 59.340"
Primary Width	208 mm	Altitude	1044.2 m asl
Primary Weight	575 kg	IAU-MPC	043
Primary Length	6000 mm		
Primary Focal Ratio	f/5.0		
Secondary Diameter	520 mm		
Eq. Focal Length	12100 mm		
Focal Ratio	f/10.1		
Telescope Scale	17.05 arcsec/mm		

Grating Set				
Grating-type	Blaze Angle	Blaze λ	Dispersion	
gr/mm	° '	Å	Å/mm	Å/px
150	2 09	5000	328.5	4.43
300	4 18	5000	166.8	2.25
600	8 38	4500	85.2	1.15
1200R	16 16	4000	44.3	0.60
1200B	26 45	6825	44.3	0.60

Table 3.1: *Galileo telescope specifics.*

3.3 Dataset

3.3.1 The Asiago Comets

The idea for this thesis came from the Asiago Atlas of Comets project, which began in 2013 with observations of comet ISON (C/2013 S1) spectra and is still ongoing. The Atlas adhere to a long-dated tradition of cometary spectra observations at the Asiago Observatory, which began from its very inauguration, in 1942. The purpose is to make available an accurate series of high-quality data to the scientific community.
The Asiago spectral sample provides an excellent opportunity to study the diversity of comets across various dynamical groups. Validating a substantial dataset obtained from the Galileo telescope, compact yet highly efficient, opens up extensive possibilities for the ongoing monitoring of comets.

The full sample, updated to 2023-11-22, is composed of 38 comets. For the purpose of this thesis, the sample was reduced to 27, discarding those spectra having a signal-to-noise too low to correctly perform the analysis.

The comets were observed mainly with the 300 lines/mm grating covering the region from 3300 to 7900 Å, while for 67P Chyuriumov-Gerasimenko, 12P Pons-Brooks were collected spectra with the 1200 lines/mm grating in the blue region, from 3820 to 5020 Å. The slit width variated from 150 μm to 600 μm. The full sample analysed is reported in Tab. 3.2, containing information about every comet's perihelion and dynamical group. In Tab. 3.3 are reported observational specifics of the sample.

3.3.2 Peculiar Comets

The sample analysed includes comets belonging to all four principal dynamical groups: JFC (Jupiter Family Comets), HT (Halley Type), R (Returning) and DN (Dynamically New). Among them, there are certain objects widely known and documented in the literature for their peculiarities.

Comet **12P Pons-Brooks** is periodically subject to outburst events, which are sudden in-

creases of the luminosity by 2-5 magnitudes (Wesołowski et al., 2020a), and three of these events are covered in our dataset.

Comet **67P Churyumov-Gerasimenko** underwent an outburst event too, but this is not the main reason why it is largely known. This is indeed the comet visited by the Rosetta mission on 6 August 2014, witnessing the first-ever comet landing in history.

19P Borrelly was a bonus fly-by executed by Deep Space One probe thanks to an unexpected prolongation of the mission program. This object is known for its highly asymmetric dust coma shape and a prominent jet feature coming from its nucleus (Boice et al., 2002), Section 4.2.

46P Wirtanen is a JFC comet having a nucleus size below 1 km, and was the initially designed target of the Rosetta mission. It belongs to the category of hyperactive comets (Rickman and Jorda, 1998), meaning a very high fraction of the surface actively outgasses, even producing more water abundance with respect to the one imputable to the sublimation from the nucleus. This phenomenon was explained by A'Hearn et al. (2011) as the sublimation of CO_2 dragging grains of water ice into the coma, from which originates the additional outgassing.

Comets **C/2012 S1 ISON** and **C/2019 Y4 ATLAS** both underwent disgregation events. For ISON it occurred during its perihelion, on November 28, 2013, leaving behind a much-reduced nucleus enclosed in a dust debris cloud. While Y4 was observed by the Hubble Space Telescope after its fragmentation into over 30 components on April 20-23, 2020, way before reaching the perihelion.

C/2017 K2 PanStarrs, as mentioned in Section 1.1, was one of the comets whose activity was documented at record heliocentric distance. This one has a large nucleus, whose dimensions were measured around 9 km (Jewitt et al., 2017). The presence of a massive nucleus is something usually noticed in all comets found active at large heliocentric distances.

Comet **C/2020 F3 NEOWISE** is known as one of the brightest comets visible in the northern hemisphere, since the crossing of comet Hale-Bopp in 1997. This comet reached a visual magnitude of 0.5–1 mag making it visible to the naked eye (Munaretto et al., 2023).

Name	Perihelion date [yyyy-mm-dd]	r [AU]	Δ [AU]	Dynamical Group
12P	2024-04-21	0.78	1.61	HT
19P	2022-02-02	1.31	1.27	JFC
38P	2018-11-11	1.59	1.31	HT
46P	2018-12-16	1.06	0.08	JFC
67P	2021-11-02	1.21	0.42	JFC
104P	2022-01-12	1.07	0.66	JFC
123P	2019-02-05	2.13	1.26	JFC
156P	2020-11-17	1.33	0.52	JFC
C/2012 S1	2013-11-28 [a]	0.08	0.96	DN
C/2013 US10	2015-11-16	0.82	1.74	DN
C/2013 X1	2016-04-21	1.31	1.96	DN
C/2015 V2	2017-06-12	1.64	0.82	DN
C/2016 N6	2018-07-18	2.67	3.65	R
C/2017 K2	2022-12-20	1.80	2.48	DN
C/2017 T2	2020-05-04	1.62	1.70	R
C/2018 N2	2019-11-11	3.11	2.31	DN
C/2018 Y1	2019-02-07	1.29	0.38	R
C/2019 L3	2022-01-10	3.55	2.58	DN
C/2019 Y4	2020-05-31 [b]	-	-	R
C/2020 F3	2020-07-04	0.30	1.14	R
C/2020 M3	2020-10-26	1.27	0.40	HT
C/2020 R4	2021-03-21	1.03	1.71	R
C/2020 T2	2021-06-11	2.06	1.67	R
C/2020 V2	2023-05-08	2.23	3.22	DN
C/2022 E3	2023-01-13	1.11	0.70	DN
C/2023 E1	2023-07-01	1.03	0.65	HT
C/2023 H2	2023-10-29	0.89	0.50	R

Table 3.2: *Full sample of comets from the Asiago Atlas used for the study of CN production rate. For every comet are reported date, heliocentric and geocentric distances in correspondence of its perihelion. The dynamical groups are shortened as JFC (Jupiter Family Comets), HT (Halley Type), R (returning) and DN (Dynamically New).*
[a]*: The comet disgregated during perihelion on 2013-11-28*
[b]*: The comet disgregated before perihelion on 2020-03-22*

| Name | Date | Observation Geometry | | | | Slit | exptime | airmass | Solar |
	[yyyy-mm-dd]	r [AU]	$\dot{r}$ [km/s]	Δ [AU]	ϕ deg	[μm]	[s]		Analog
12P (Pons-Brooks)	2023-11-18	2.54	−20.91	2.73	21.3	200	180	1.35	16 Cygni B
19P (Borrelly)	2022-01-23	1.31	−1.73	1.23	45.4	200	900	1.60	Land 93m108
38P (Stephan-Oterma)	2019-01-05	1.74	8.62	0.80	15.0	200	1800	1.04	Land 98m978
46P (Wirtanen)	2019-01-06	1.10	7.00	0.15	33.2	200	1200	1.41	Hyades 64
67P (C-G)	2022-01-10	1.48	11.58	0.52	13.1	200	1800	1.18	Land 102m1081
104P (Koval 2)	2022-01-30	1.10	5.44	0.64	62.2	200	900	1.55	Hyades 64
123P (West-Hartley)	2019-02-17	2.13	0.61	1.21	12.9	250	1800	1.22	16 Cygni B
156P (Russel-Linear)	2020-11-20	1.33	0.53	0.54	40.2	200	1200	1.73	Hyades 64
C/2012 S1 (ISON)	2013-11-07	0.84	−45.57	1.07	61.2	250	1800	2.46	Land 102m1081
C/2013 US10 (Catalina)	2016-01-21	1.44	22.98	0.74	39.2	200	600	1.06	Land 102m1081
C/2013 X1 (PanStarrs)	2016-01-06	2.00	−17.45	1.88	29.1	200	600	1.38	Land 102m1081
C/2015 V2 (Johnson)	2016-11-30	2.94	−16.37	2.98	19.2	200	1200	1.44	Land 102m1081
C/2016 N6 (PanStarrs)	2019-01-06	3.21	9.66	2.41	11.8	200	1800	2.43	Hyades 64
C/2017 K2 (PanStarrs)	2022-05-20	3.12	−15.54	2.38	14.7	200	900	1.22	Land107m684
C/2017 T2 (PanStarrs)	2020-05-02	1.62	−0.42	1.70	35.2	250	600	1.38	Land 107m684
C/2018 N2 (ASASSN)	2019-09-23	3.16	−2.48	2.34	12.3	200	1800	1.04	Land 115m271
C/2018 Y1 (Iwamoto)	2019-02-21	1.31	4.47	0.46	39.0	200	1800	1.17	Land 98m978
C/2019 L3 (Atlas)	2022-01-06	3.55	−0.11	2.58	2.6	200	1200	1.07	Hyades 64
C/2019 Y4 (Atlas)	2020-04-10	1.29	−33.21	1.01	49.1	250	1800	1.33	Land 107m684
C/2020 F3 (Neowise)	2020-07-30	0.81	37.38	0.77	80.0	200	300	2.32	16 Cygni B
C/2020 M3 (Atlas)	2020-11-12	1.30	5.42	0.36	27.5	222	1800	1.38	Hyades 64
C/2020 R4 (Atlas)	2021-04-24	1.36	17.70	0.47	35.2	200	1800	1.05	16 Cygni B
C/2020 T2 (Palomar)	2021-03-31	2.38	−10.02	1.55	16.8	200	1800	1.13	Land 102m1081
C/2020 V2 (ZTF)	2023-08-11	2.48	8.54	2.18	24.1	200	300	2.32	16 Cygni B
C/2022 E3 (ZTF)	2022-08-22	2.39	−19.93	2.15	24.9	200	900	1.23	16 Cygni B
C/2023 E1 (Atlas)	2023-06-25	1.03	2.39	0.67	69.7	200	1200	1.28	Land 107m684
C/2023 H2 (Lemmon)	2023-11-12	0.90	−2.59	0.63	100.3	150	600	1.58	16 Cygni B

Table 3.3: *Here are reported the main observational details about the sample. From left to right are the observation date, the heliocentric distance r, heliocentric velocity $\dot{r}$, geocentric distance Δ, sun-comet-observer phase angle, slit width, exposure time and solar analog used for removing the dust continuum. The information on r, $\dot{r}$, Δ and ϕ are taken from JPL Horizon service* `https: //ssd.jpl.nasa.gov/horizons/`.

3.3.3   My Contribution: Computation of CN Production Rate

As part of my research, I conducted observations of comets from June to November 2023, actively participating in most of the observational sessions. Afterwards, I reduced the acquired data, deriving values for the CN production rate specifically for the (0-0) line of the violet system from the integrated fluxes.

Among the comets observed during this period, there were three particularly interesting objects, 12P, C/2023 E1, and C/2023 H2. For these comets, I personally reduced the data using IRAF software, implementing a non-standard reduction and analysis procedure tailored to the distinct data type and the scientific purposes. A detailed individual analysis of these comets is presented in Section 4.2.

Upon joining the Asiago Comets Atlas project, the sample comprised 33 items, each with spectra reduced using a semi-automatic IRAF-based pipeline specific to the 1.22m Galileo telescope. Multiple spectra were collected for each comet every night, weather permitting. Additionally, standard star spectra were taken for flux calibration (see Section 3.5.4), and a solar analog spectrum was acquired to eliminate the contribution of the Sun (Section 3.6).

Originally designed to prove the 1.22m telescope's capability to obtain high-quality spectroscopic data, even for challenging objects such as comets, the primary objective of the Atlas project was not to measure gas production rates. Consequently, I adapted the Haser model for calculating the CN production rate based on the available data (see Section 2.2.1). Furthermore, I evaluated the introduced error in the calculated flux, assuming a uniform brightness profile along the comet's coma due to the absence of the actual luminosity trend. This aspect is elaborated further in Section 3.8.

Finally, I developed a Python-based code designed to compute the CN (0-0) integrated band flux and convert it into production rates, using the reduced spectra as a foundation. The underlying physics of this code is based upon the works of Fink and Hicks (1996), Cochran et al. (2012), Schleicher (2010), and Venkataramani et al. (2016).

3.4   Challenges in Observing Comets

Observing comets presents various challenges, making their observations requiring different tactics to obtain high-quality results.

- **Faintness and Background Distinction:**
  Comets typically present as faint sources against the background of the night sky. Distinguishing them from the sky background represents the first significant challenge.

- **High Velocity and Manual Tracking:**
  Comets frequently display rapid motion during observations, and the telescope's automatic tracking system struggles to accurately follow their trajectory. Consequently, manual adjustments are necessary during exposures, assisted by supplementary engines. Additionally, it's important to note that the telescope's auto-guidance system is not designed to track objects within the observation slit. Hence, ensuring the comet stays within the designated slit requires vigilant monitoring during the exposure.

- **Diffuse Coma and Spectral Aperture Selection:**
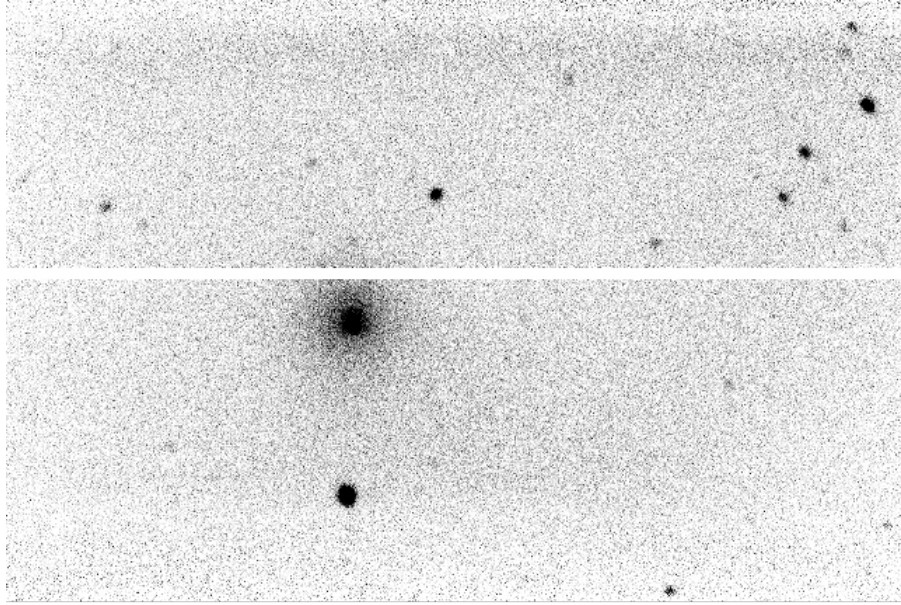 The presence of a diffuse coma around comets complicates the determination of an optimal

Figure 3.1: *Galileo EMCCD guiding camera image of comet C/2020 V2. The slit position is indicated by the central white strip. The comet's position must be adjusted during the exposure, maintaining it inside the slit.*

spectral aperture size. The final goal is to capture the most of comet's signal while minimizing interference from the sky background.

- **Sky and Comet Oxygen Lines Overlap:**
  Comet optical spectra exhibit O[I] spectral lines, including the most intense ones at 6300 Å and another at 5577 Å. However, identifying the source of emission is challenging because these lines overlap with the auroral oxygen lines. Additionally, the sodium doublet may originate from both the comet and the sky pollution, especially night lamps. It is rare to observe sodium in comets, making unobstructed observations even more essential.

- **Band Flux Filling the Slit Width:**
  Certain spectral lines, like the violet CN band, exhibit intense flux, spreading across the slit width and impeding accurate extraction of the sky background. Addressing this challenge involves employing multiple short exposures to control the amount of flux entering the slit.

- **Dust-Induced Spectrum Contamination:**
  Comets are not only composed of gas but also contain dust. The sunlight reflected from comet dust can introduce a reddened solar continuum into the spectrum, distorting the emission bands flux measurements. To remove the solar component, nightly observations of a solar analog star are needed, allowing the removal of dust-induced contributions from the comet's spectrum. More details of the dust removal procedure are provided in Section 3.6.

3.5 Data Reduction

In this section, it is explained how the flux integral of the CN $\Delta\nu = 0$ violet band is obtained from raw images. The first part of the process involves reducing the raw images using IRAF software. Next, the flux integral of the band is computed by assuming its shape as the superposition of two Gaussian functions. Finally, it is shown the procedure to convert fluxes into molecular production rates within the Haser model, as seen in Section 2.2.

3.5.1 Correcting for the Instrumental Noise

Before starting to make considerations on the flux received from the source, it is essential to remove the instrumental issues introduced by the characteristics of the CCD. The main points are the bias level, the pixel response inhomogeneity and the dark current. In this section I will describe in detail the IRAF standard procedure, calling the name of some tasks. The overall procedure I followed while reducing the data is mostly similar to what the pipeline does. Any differences will be specified.

- **Bias**:
  This effect is an artificial count value introduced by the CCDs manufacturer to avoid registering negative photon counts during exposure. This quantity is called bias level, it is a constant and its value is usually known and made available to whoever uses the CCD. What is missing is the statistical fluctuations around this value, which is the read-out noise of the CCD. There are two ways of estimating the bias level and the read-out noise. The first approach is to take so-called bias frames: these are images collected with the shutter closed and a null exposure time. The second way is to use the overscan region, a covered pixel section which is not hit by photons. Both approaches are meant to measure the average ground level of the CCD counts and the standard deviation of this quantity. Finally, the bias level is subtracted from the scientific frame.
  While personally reducing the data I used the bias frame; the pipeline uses the overscan instead.

- **Flat-fielding**:
  Another source of error is given by the difference in every pixel response to the same amount of radiation. This is another structural deficiency of the CCD. The correction applied to this effect is called flat-fielding. A flat image is made by illuminating uniformly the CCD through a quartz lamp whose spectrum has no emission lines. Several flat images are taken and then mediated. To obtain the percentage response difference between the single pixels, the median flat has to be normalized to unity. While in photometry the use of a filter limits wavelength dependencies in the illumination, this is not true for spectroscopy. This makes the flat frames not actually uniform. There are two ways to correct this effect for spectroscopic flats:

  - **Using `blkavg` and `blkrep`**:
    Briefly, first `blkavg` produces an image with the initial number of columns and a single row, containing the median value of the pixels in every column. Then `blkrep` replicates these values for the initial number of rows, producing a final image with the same dimension as the initial flat.

  - **Using `response`**:
    `response` does a fit of the variation in the pixel response with the wavelength along the median flat, then uses it to correctly normalize the median flat.

  These are simply different ways to deal with the same problem and have both been used while reducing the data. By looking at a flat-field image an effect of the B&C Asiago spectrograph

is immediately noticed: the fringing effect. The fringe pattern is typical of thin sensors and is caused by interference between the incident light and reflected light in the inner layers of the sensor. This is not affecting the analysis here pursued, as it occurs up to $\lambda > 7000$ Å, but it can be a major problem if studying IR emissions.

- **Dark**:
  The dark current is defined as the thermo-electrons flowing through the CCD during the exposure, produced by the thermal agitation of the CCD electrons. Nowadays professional instrumentation such as the one used in Asiago, has ways of treating of this error by cooling the CCD to $\sim -73°$. In any case, it is always a good idea to take dark frames, in particular if the exposure time of the science frames is higher than 20 minutes. In this case, five dark frames are enough to have a good statistic. A dark frame is taken with the shutter closed and an exposure time equal to the one of the scientific frame. To correctly scale a dark exposure time to the scientific images, the following IRAF procedure is used: `darkcombine` task to do the median the dark frames, taking care of setting the `scaling` parameter to `exposure`. Then use `ccdproc` with the only `dark` correction switched on. In this way, IRAF autonomously scale the median dark for the correct exposure.

- **Trim**:
  The final "instrumental" step is the cut of the overscan region. It is sufficient to display a flat image and detect the edges of the illuminated area in both the x and y directions. Then this region has to be written in the parameters of `ccdproc` task, specifying in the `trimsec` parameter the effective area, in this format [$x_{eff,min}$:$x_{eff,max}$, $y_{eff,min}$:$y_{eff,max}$]. After this step, the actual pixel region is the one corresponding to the only light coming from the sky.

Now the frames are almost ready for their scientific purpose. It is left to tune photon counts to flux units and pixels to wavelength units.

3.5.2 Wavelength Calibration

As the B&C spectrograph has the dispersion direction along the rows, and slit width along the columns, these two terms are in this place used as a synonym for dispersion direction (row) and slit direction (column). The dispersive element of the spectrograph will show, along the rows, an image representing the amount of light incoming in each wavelength bin (given by the spectrograph resolution). But the CCD has no way of knowing the wavelength value in Å at which every count is registered, rather it will give the information in effective pixels covered. To know how many Å fit in a pixel it is necessary to take the spectrum of an emission arc lamp with tabulated emissions. IRAF has its procedure to compare the emissions in this frame with the rows in the scientific frame. The first two steps are meant to find the dispersion solution for the spectrum, giving the amount of wavelength units for each pixel. The last two correct the slit image curvature.

- `identify`:
  This is an interactive procedure to obtain the dispersion solution for the arc lamp spectrum. The command opens a graphic window showing a single dispersion line, namely the central line of the image. Every line should be identified by eye using a comparison line map for that specific lamp with the same spectral set-up. In the graphical window, the most evident lines may be marked and their laboratory exact wavelength inserted. It is enough to mark 4 or 5 strong lines. Then IRAF does a fit with a polynomial function that determines the best fit for the input line with a dispersion solution [Å/pixel]. This fit can be improved by uploading the information contained in a line list (text file to be given as input). Care should be taken in giving input to the file containing the exact wavelength of every emission line. It is always

better for observers to produce the line maps file themselves, with the aid of an emission line atlas, instead of using the one contained in IRAF's directory (`page linelist$README`), as lower residuals are achieved. I produced the coordinates file with the aid of the arc lamp line atlas available at the Asiago Observatory website[2].

- `reidentify`:
  What has been done by `identify` for a single CCD column is now extended to the whole slit width. The identification is automatically repeated for every row along the slit direction. The task can be set in interactive mode to adjust the fit applied to every single row.

- `fitcoords`:
  The dispersion solution is used to apply a two-dimensional polynomial function to fit the solution to the whole image. This task allows the user to view and correct the tracing of the dispersion solution along the slit width. It is possible that the tracing fails to follow all the lines detected along some rows. To avoid introducing distortions in the final image, these rows should be detected and manually removed.

- `transform`:
  Last step applies the fit to the input image. If the procedure is successful, an image that is rectified and calibrated will be obtained.

3.5.3 Spectrum extraction
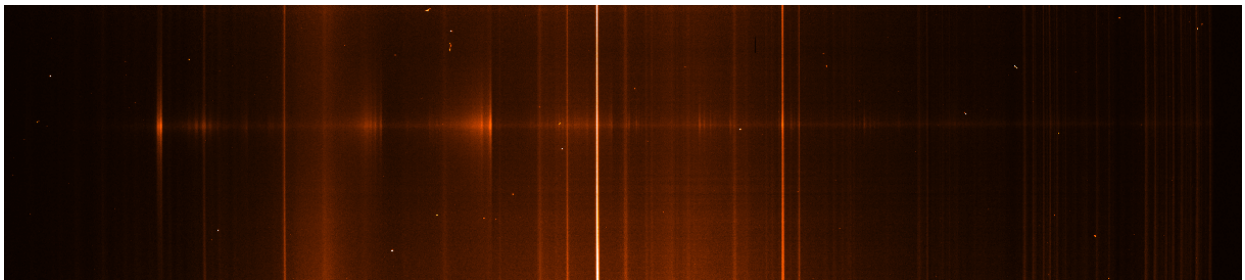
Figure 3.2: *Bidimensional spectrum of comet C/2023 E1 ATLAS. CN (0-0) transition, C_3 and C_2 Swan bands are visible. Corrections for bias, flat, dark and wavelength calibration are applied. Strong sky lines are still visible as the sky subtraction step is done along with the spectrum extraction (Section 3.5.3). 300 lines/mm grating, 150 µm slit. 2023-06-25, 1.22m Galileo telescope, Asiago Observatory.*

From the two-dimensional frame (Fig. 3.2), the final monodimensional spectrum is extracted by summing the flux measured at the same wavelength along the slit direction. The extraction is performed using the task `apall`, a quite versatile command which is the result of merging different tasks. Briefly, `apall` allows the user to:

- Take a section of the wavelength axis to detect the position of the source in the slit

- Locate the centre of the spatial cometary profile and set the upper and lower limits of the extraction aperture

- Indicate a region onto which to fit the background by using polynomial functions

- Trace the given aperture along the whole wavelength axis

---

[2]`https://www.astro.unipd.it/inglese/observatory/`

All of this is manageable interactively through a graphic window.

The aperture's radius and the slit width together determine the effective area for measuring the final flux. When extracting a stellar source, the size of the aperture is not much debatable, as its shape is simply a point spread function. The extraction follows the peak of the emission and neglects the region of the wings, near the continuum. However, if the object is a comet, the process becomes more complex due to the presence of the coma around the phototocenter. Additionally, comets are often faint sources, making it difficult to distinguish the coma flux from the background. For every specific case, the solution gaining the maximum flux from the source is evaluated by varying the aperture and choosing the one producing the cleanest spectrum (details in Fig. 3.3). Once the aperture has been determined, `apall` lets the user choose which slit-section contains only the background, by setting the parameter `background` to `fit`. When extracting cometary spectra, one does not want to select these sections too near the comet's flux, to avoid subtracting part of the coma with the background. Finally, the program traces the object by attempting to find the centre of the spatial profile in all the other columns of the image, until reaching the edges or losing the trace.

3.5.4 Flux calibration

The last calibration step is the conversion of photon counts to flux units: erg cm^{-2} s^{-1} Å^{-1}. In this case, the reference spectrum is a spectroscopic standard star, which spectrum has to be observed every night. A spectroscopic standard star is a bright source whose precise flux values are tabulated. These tabulated values may be consulted upon the ESO website (`https://eso.org/sci/observing/tools/standards/spectra.html`) where are available file text both in magnitude or flux units. For certain stars, the flux files are already present in IRAF internal directories[3]. If the reference star cannot be found in this list, the magnitude file has to be retrieved from ESO website and specified in `standard`'s settings. The scope of the calibration is to gain the instrumental luminosity response curve, which comes from the ratio between the count value measured by the CCD at every wavelength bin and the standard tabulated values. IRAF standard procedure is made of three steps:

- `standard`:
  This task is aimed at resampling the reference spectrum observed to make it comparable with the tabulated fluxes. The output is a text file containing the counts in ADU registered in each wavelength band, together with the corresponding flux value. To improve the result of the fit in the next step, it is suggested to remove the wavelength bins placed over the absorption lines and sample only the continuum region. In fact, in the region of the absorption lines the ratio between tabulated and observed fluxes deviates from the overall trend, and the risk of compromising the fit is high.

- `sensfunc`:
  Fits with a polynomial function the values of the ratio for every bin. Gives in output the response curve of the instrument. If the absorption features have not been removed in the previous step, the fitting function has to manage various outlier points.

- `calibrate`:
  Applies the calibration to the input image(s) specifying the sensitivity function. This task includes the possibility of applying extinction correction by providing an extinction curve of the observatory.

---

[3]The full list of spectroscopic standards available in IRAF can be found in `http://stsdas.stsci.edu/cgi-bin/gethelp.cgi?onedstds`.
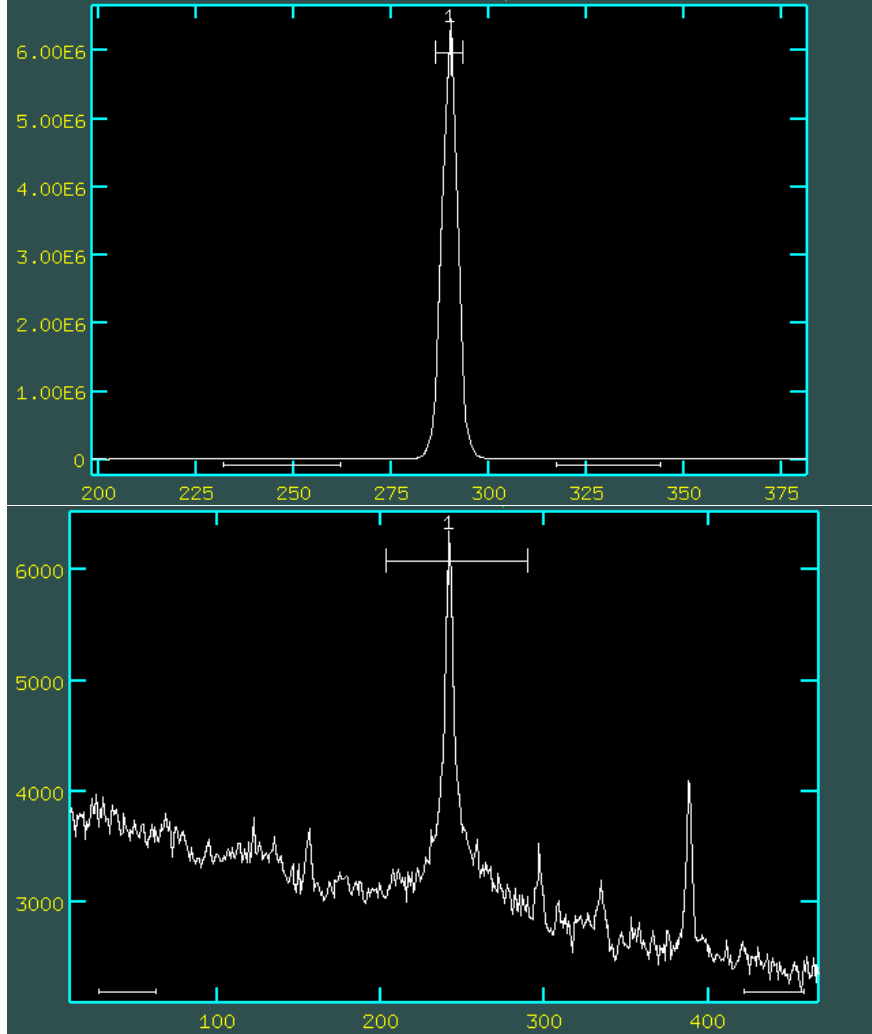
Figure 3.3: *The difference between the intensity profile of the solar analog 16 Cygni B (upper) and the comet C/2023 E1 (lower). In the plots are visible the upper segment, which is the spectral aperture, and the two lower segments, which are the regions selected to extract the sky contribution. It is evident the difference in signal-to-noise ratio and the symmetry of the profile with respect to the photocenter. While the star has a high S/N, a symmetric profile and there is not much decision about where sky region to select, the comet is visibly fainter, surrounded by an asymmetric coma and the sky must be taken not too close to the photocenter (to avoid removing the coma contribution) and also care must be taken to not include other sources included in the slit.*

3.6 Removing the solar spectrum

Each cometary spectrum is the combination of the gas emission features and the reflectance spectrum of the dust particle, which typically has the shape of a reddened solar spectrum. To remove the dust component to analyse the gas emissions it is necessary to have a reference spectrum of the Sun and then divide this reference from the comet spectrum. Whenever a comet was observed, also a solar analog star spectrum is taken, as closest as possible in coordinates, airmass and with the same slit width as the comet. A detailed list of solar analogs is reported in Tab. 3.4. The solar analog flux is normalized to its peak of flux emission, 5500 Å. In this way the division does not alter the comet's flux. In Fig. 3.4 the spectrum of one of the most used solar analog in the survey, Land98m978, is shown.
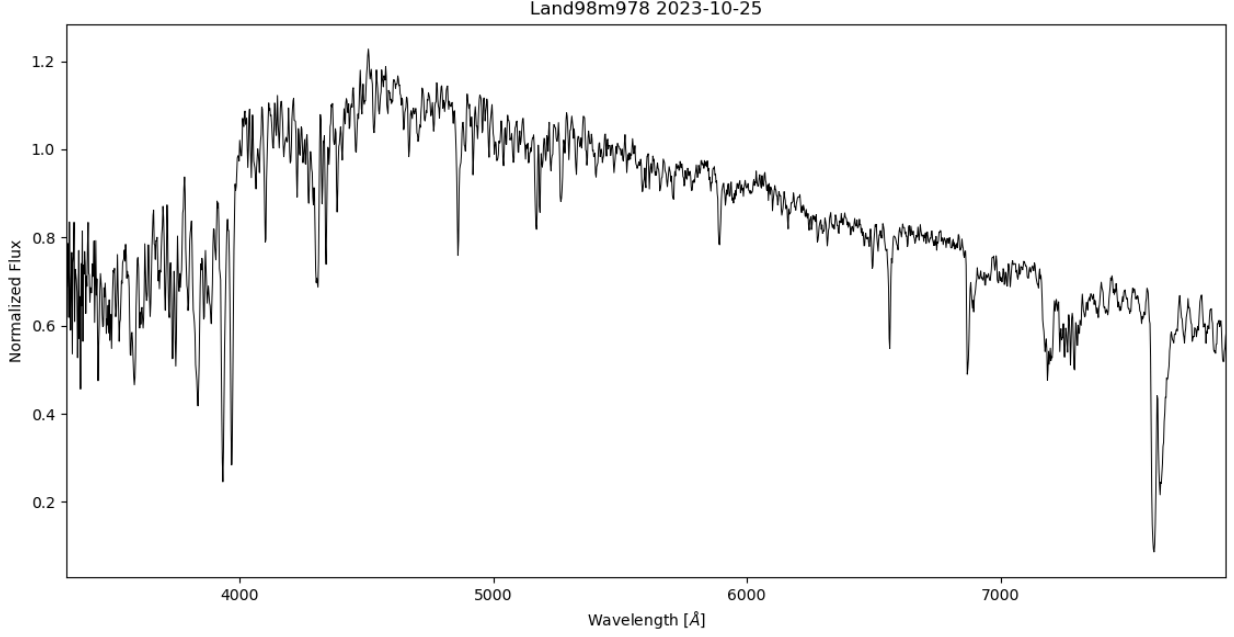
Figure 3.4: *Spectrum of the solar analog Land98m978. The flux is normalised at 5500 Å. 1.22m-Galileo 2023-10-25.*

Solar Analog	RA	DEC	M_V
	[hh mm ss]	[°' "]	mag
Land (SA) 93-101	01 53 18.0	+00 22 25	9.7
Hyades 64	04 26 40.1	+16 44 49	8.1
Land (SA) 98-978	06 51 34.0	−00 11 33	10.5
Land (SA) 102-1081	10 57 04.4	−00 13 12	9.9
Landolt (SA) 107-684	15 37 18.1	−00 09 50	8.4
Land (SA) 107-998	15 38 16.4	+00 15 23	10.4
16 Cygni B	19 41 52.0	+50 31 03	6.2
Land (SA) 112-1333	20 43 11.8	+00 26 15	10.0
Land (SA) 115-271	23 42 41.8	+00 45 14	9.7

Table 3.4: *List of solar analog stars ordered for right ascension used to remove the dust reflectance spectrum.*

3.7 Data Analysis

Here is discussed the procedure leading to the final result, which is a value for the molecular production rate Q in mol s^{-1} of CN $\Delta\nu = 0$ emission band at 3875-3883 Å. The first step is collecting the whole flux within the CN violet emission band. The distinguishable shape of the CN $\Delta\nu = 0$ band is a two-peak feature which is the result of a low-medium resolution spectrum of the transitions between the ground electronic levels of CN: $B^2\Sigma^+$ - $X^2\Sigma^+$ (a deeper explanation is provided in Section 2.1.1).

To collect the flux underlying the curve, the emission band is fit with the combination of two Gaussian profiles (Fig. 3.5). The continuum near the emission band ($\sim 3600 - 3920$ Å) is fitted with a first-order cubic spline polynomial function. The continuum region is more extended at $\lambda < 3880$

Å in order to avoid being contaminated from the C_3 cometary band and the solar Calcium H-K doublet. The fit is performed by Levenberg-Marquardt algorithm and least squares statistic, which returns, after 5000 iterations, the best-fit values for the peaks, mean and width of the Gaussians. The integrated flux is calculated as

$$Flux = peak_{bestfit} \cdot mean_{bestfit} \cdot \sqrt{2\pi} \tag{3.1}$$

and its error as

$$\Delta_{Flux} = Flux \sqrt{2\pi \left(\frac{\Delta_{peak}}{peak}\right)^2 + \left(\frac{\Delta_{width}}{width}\right)^2} \tag{3.2}$$
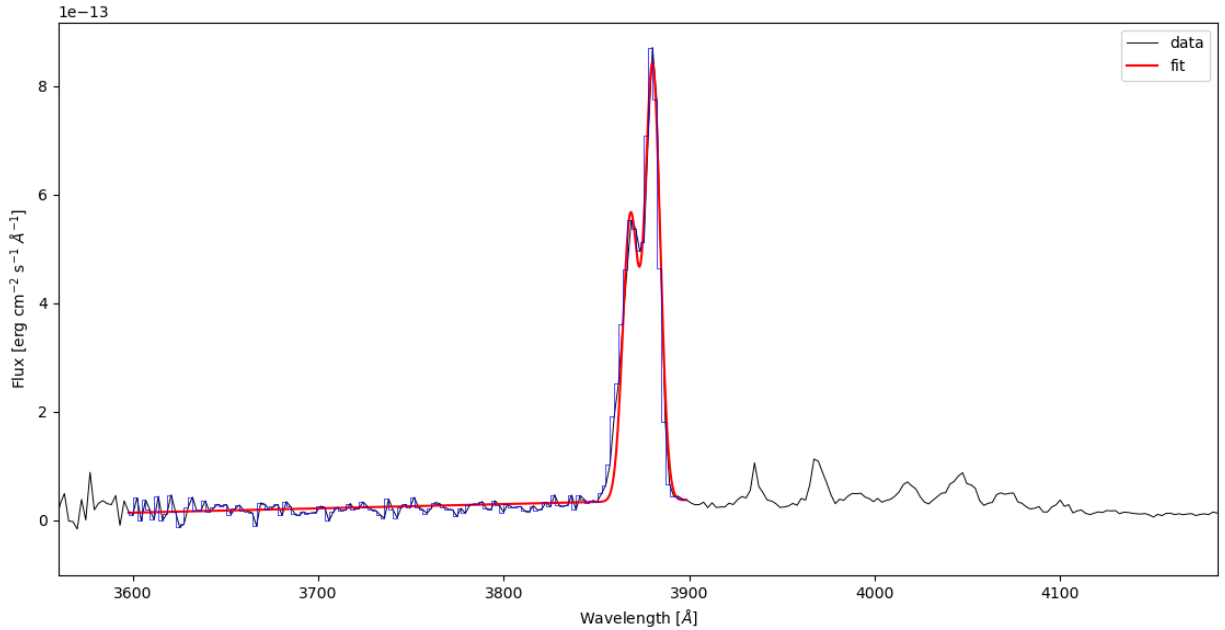
Figure 3.5: *3560-3900 Å region of the C/2023 H2 spectrum of 2023-10-25. Result of the double Gaussian fit over the CN $\Delta\nu = 0$ emission band.*

3.8 Flux of a Circular Aperture

As explained in section 2.2, the integrated flux is measured with the purpose of computing the CN production rate in the framework of a simple Haser model (Haser, 1957). The model calculation is based on gaining the total count of emitting species on the whole comet's coma, starting from the amount of flux collected within the aperture. The approach here used is based on the work by Venkataramani et al. (2016) where they adapted their longslit aperture to an analogous circular aperture.

The flux collected within the long-slit aperture, F_{long} is divided by its effective area, given by multiplying the slit width, s, by the spectral extraction aperture, a. Then the flux per unit area is multiplied by the area of a circular aperture having the same radius as the initial spectral aperture, as in Eq. 3.3.

$$F_{circ} = \pi a^2 \cdot \frac{F_{long}}{s \cdot a} \tag{3.3}$$

3.8.1 Approximation Introduced

Despite the conversion from long-slit to circular aperture is necessary to employ the Haser model, it introduces a significative approximation. In fact, it does not consider the decaying of the coma luminosity with the increasing nucleocentric distance. By multiplying the flux for the circular area, the result is an overestimation of the real flux of the coma, given by diluiting the naturally brighter flux of the photocenter to the whole aperture.

The solution to this issue would follow these steps:

- Extract the same spectrum with different apertures, with at least one small ($\sim$ 10 arcsec) window including only the photocenter flux.

- Measure the flux per unit area of the photocenter spectrum

- Subtract the photocenter spectrum from the other wider apertures. In this way the actual measured flux is the flux of an annulus $\sim$ 5 arcsec distant from the nucleus

- Convert the flux of the annulus to the correspondent circular aperture, as explained above

- Re-add the photocenter flux.

Following these steps would solve the overestimation issue. Sadly, these considerations could be done only after I began working on the spectra and I had no way of modifying the apertures of the old data.

To address the issue at hand, I utilized the raw spectra of comets 12P and C/2023 E1 to calculate the degree of overestimation and obtain a more accurate estimate of the reliability of fluxes obtained from previous data. Subsequently, I applied the previously explained approach to comets that I personally observed, based on the established solution.

The result on the spectra of comets 12P and C/2023 E1 is that the entity of the overestimation decreases with the spectral aperture. For apertures larger than 40 arcsec, the flux overestimation is below 20%. The typical aperture over which a comet is observed beyond 50-60 arcsec. Given that, in the end, the error resulting from not considering the true profile of the CN band along the coma is between the margin of error given by the Gaussian fitting procedure.

3.9 From integrated fluxes to production rates

The integrated fluxes are converted to production rates by using the procedure from (Fink and Hicks, 1996), better explained in Section 2.2. The equation is:

$$Q = \frac{4\pi\Delta^2 \cdot v_{out}}{g \cdot l_d} \cdot Flux \cdot HC \tag{3.4}$$

Where Q (mol s^{-1}) is the molecular production rate, Δ (km) is the Geocentric distance, g (erg s^{-1} mol^{-1}) is the fluorescence efficiency (Schleicher, 2010), l_d (km) is the parent scale length, Flux (erg cm^{-2} s^{-1}) is the total integrated flux and HC is the Haser Correction. $4\pi\Delta^2$ is the radiation dilution factor. The scale length set used was the one published by Randall et al. (1992). The CN fluorescence efficiency are those computed by Schleicher (2010). Finally the Haser Correction was computed with the aid of Schleicher's softwere, available on the Lowell Observatory website[4]. Tab. 3.5 contains all the parameters used for the calculation of production rates.

---

[4]https://asteroid.lowell.edu/comet/intro

Name	r [AU]	$\dot{r}$ [km/s]	Δ [AU]	g-factors $[10^{-13}$ erg s^{-1} mol$^{-1}]$	l_p $[10^4$km]	l_d $[10^5$km]
12P	3.85	−17.83	3.54	0.260	19.269	31.127
19P	1.31	−1.73	1.23	1.670	2.230	3.604
21P	1.03	−4.26	0.42	3.100	1.379	2.228
38P	1.74	8.62	0.80	1.520	3.936	6.358
46P	1.10	7.00	0.15	3.950	1.573	2.541
67P	1.48	11.58	0.52	2.010	2.848	4.600
104P	1.10	5.44	0.64	3.880	1.573	2.541
123P	2.13	0.61	1.21	0.600	5.898	9.528
156P	1.33	0.53	0.54	1.530	2.300	3.715
C/2012 S1	0.84	−45.57	1.07	5.160	0.917	1.482
C/2013 US10	1.44	22.98	0.74	1.740	2.700	4.355
C/2013 X1	2.00	−17.45	1.88	0.898	5.200	8.400
C/2015 V2	2.94	−16.37	2.98	0.406	11.237	18.152
C/2016 N6	3.21	9.66	2.41	0.429	13.395	21.639
C/2017 K2	3.12	−15.54	2.38	0.345	12.655	20.442
C/2017 T2	1.62	−0.42	1.70	1.010	3.412	5.511
C/2018 N2	3.16	−2.48	2.34	0.321	12.981	20.970
C/2018 Y1	1.31	4.47	0.46	2.560	2.231	3.604
C/2019 L3	3.55	−0.11	2.58	0.219	16.383	26.465
C/2019 Y4	1.29	−33.21	1.01	2.080	2.163	3.495
C/2020 F3	0.81	37.38	0.77	6.080	0.853	1.378
C/2020 M3	1.30	5.42	0.36	2.730	2.197	3.549
C/2020 R4	1.36	17.70	0.47	2.170	2.405	3.884
C/2020 T2	2.38	−10.02	1.55	0.562	7.364	11.895
C/2020 V2	2.48	8.54	2.18	0.731	7.996	12.916
C/2022 E3	2.39	−19.93	2.15	0.686	7.426	11.995
C/2023 E1	1.03	−2.37	0.67	2.800	1.379	2.228
C/2023 H2	0.90	−2.59	0.63	3.650	1.053	1.701

Table 3.5: *The main parameters used for the computation of CN production rates are reported. From the left to the right: Heliocentric distance, heliocentric velocity, geocentric distance, fluorescence efficiency, parent scale length, daughter scale length.*

Chapter 4

Results

4.1 Overall Sample Analysis

We obtained molecular production rates for the CN violet band by integrating the flux within the emission and converting it to Q(CN) by using a simple Haser model, using the set of scale length (l_p, l_d) from Randall et al. (1992) and the fluorescence efficiencies factors (g) from Schleicher (2010), using Eq. 2.6 as described in Section 2.2.1.
The results are summarized in Tab. 4.1 with the respective heliocentric distance.

4.1.1 Validation of the Method

To validate the methods used we decided to compare the obtained results with the most close in time published values. The CN production rate increases during the inbound orbit while the comet approaches perihelion and decreases with distance, as with any cometary gas. This trend is given by different illumination and sublimation conditions encountered at different positions within the solar radiation field. An example of the dependence of Q(CN) from the heliocentric distance is reported in Fig. 4.1. For validation, we used published CN production rates within 0.25 AU from our measurements in the same inbound/outbound orbit (Kwon et al., 2023). We did not compare values across perihelion.
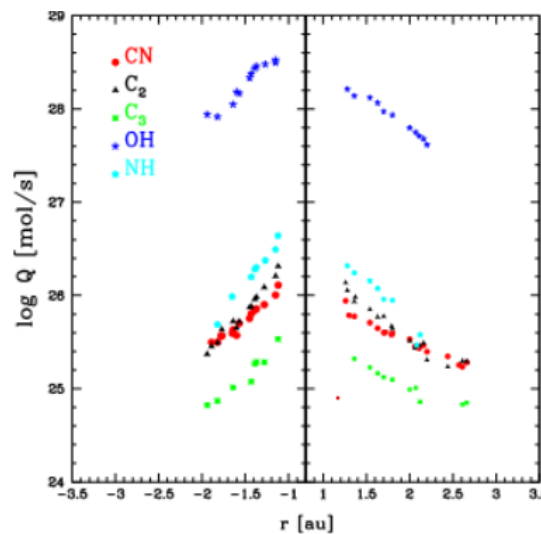
Figure 4.1: *Variation of principal cometary gases with heliocentric distance in proximity of perihelion. From Opitom et al. (2015b).*

Comet	r [AU]	Q(CN) 10^{25} s^{-1}
12P	2.61	8.77 ± 0.48
19P	1.31	6.30 ± 0.48
38P	1.74	0.31 ± 0.01
46P	1.10	1.27 ± 0.45
67P	1.48	0.64 ± 0.02
104P	1.10	1.35 ± 0.03
123P	2.13	0.17 ± 0.02
156P	1.33	0.27 ± 0.01
C/2012 S1	0.84	7.90 ± 1.77
C/2013 US10	1.44	6.78 ± 0.12
C/2013 X1	2.00	19.8 ± 0.1
C/2015 V2	2.94	6.32 ± 0.15
C/2016 N6	3.21	2.38 ± 0.30
C/2017 K2	3.12	9.30 ± 0.19
C/2017 T2	1.62	2.86 ± 0.06
C/2018 N2	3.16	0.80 ± 0.14
C/2018 Y1	1.31	0.83 ± 0.04
C/2019 L3	3.55	27.9 ± 2.8
C/2019 Y4	1.15	1.36 ± 0.17
C/2020 F3	0.81	8.03 ± 0.90
C/2020 M3	1.30	1.36 ± 0.08
C/2020 R4	1.36	1.90 ± 0.28
C/2020 T2	2.38	1.25 ± 0.86
C/2020 V2	2.48	6.57 ± 0.40
C/2022 E3	2.46	4.68 ± 0.39
C/2023 E1	1.03	0.40 ± 0.01
C/2023 H2	0.90	2.08 ± 0.05

Table 4.1: *CN violet band production rates. For comet 12P, C/2023 E1 and C/2023 H2 are reported the observations most close to the perihelion.*

The compatibility between our results and the reference one is estimated by computing the number of standard deviations between our values and the references'. The formula is the following:

$$N_\sigma = \frac{Q - Q_{ref}}{\sqrt{\sigma_Q^2 + \sigma_{Q,ref}^2}} \quad (4.1)$$

and it is the equivalent of computing the χ^2 between data points.

Values of $N_\sigma > 3$ suggest the measurements are not compatible, while $1 < N_\sigma < 2$ and $N_\sigma < 1$ indicate respectively good compatibility and high compatibility. The sample for which we found a compatible published Q(CN) within 0.25 AU comprehends eleven comets. The values of Q(CN) and heliocentric distance, both from this work and the references, are listed in Tab. 4.2, while Fig. 4.2 visualizes the residuals. What emerges is a general good agreement between Q(CN) values here computed and those obtained by other authors, with few exceptions.

After analyzing the residual plot, Fig. 4.2, it becomes apparent that there is a noticeable difference in scatter between periodic and non-periodic comets. The left side of the plot displays the behaviour

Comet	This Work		Other Authors			N_σ
	r [AU]	Q(CN) 10^{25} s^{-1}	Q(CN) 10^{25} s^{-1}	r [AU]	reference	
19P	1.31	6.30 ± 0.48	5.75 ± 0.65	1.32	(Jehin et al., 2022b)	0.68
46P	1.10	1.27 ± 0.45	1.03 ± 0.17	1.10	(Moulane et al., 2023)	1.06
67P	1.48	0.64 ± 0.02	0.61 ± 0.06	1.55	(Jehin et al., 2022b)	0.47
104P	1.10	1.35 ± 0.03	1.34 ± 0.15	1.08	(Jehin et al., 2022b)	0.07
156P	1.33	0.27 ± 0.01	0.29 ± 0.05	1.40	(Jehin et al., 2020)	0.39
C/2012 S1	0.84	7.90 ± 1.77	6.17 ± 0.19	0.72	(Knight and Schleicher, 2015)	2.18
C/2019 L3	3.55	27.9 ± 2.8	12.6 ± 1.0	3.56	(Jehin et al., 2022b)	> 3
C/2020 F3	0.81	8.03 ± 0.90	15.5 ± 3.9	0.72	(Munaretto et al., 2023)	1.87
C/2020 M3	1.30	1.36 ± 0.08	1.62 ± 0.08	1.29	(Jehin et al., 2020)	2.30
C/2022 E3	2.46	4.68 ± 0.39	2.06 ±0.16	2.24	(Jehin et al., 2022a)	>3

Table 4.2: *The table include the values of Q(CN) and r both from this work and the references. Last column contains the value of N_σ from Eq. 4.1.*
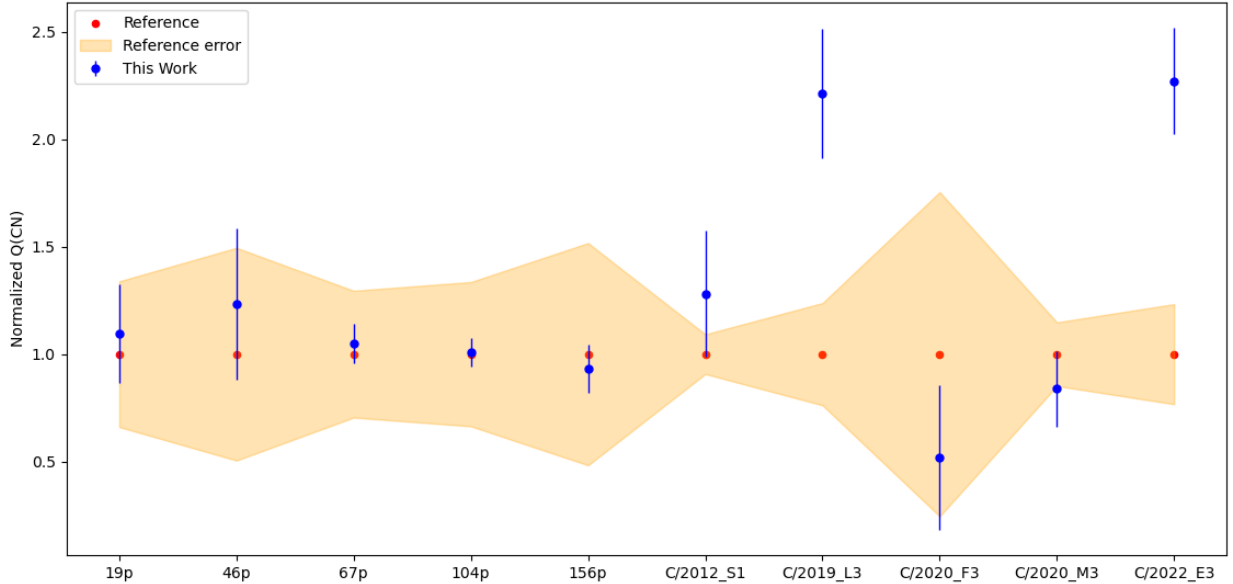
Figure 4.2: *Residual plot showing compatibility between the values of Q(CN) here obtained and results reported by other authors (detail in Tab. 4.2). The error bars and the orange region represent the 3σ errors. The percentage discrepancies are shown by normalizing our Q(CN) value to the reference values.*

of Jupiter Family and Halley Type comets, all of which show high compatibility with the findings of other authors. On the right, we can see the Returning and Dynamically New comets, and this is where the two visible outliers are located.

The compatibility values generally yield acceptable results, demonstrating that the method used in this thesis is still reliable within the uncertainties and compatible with more detailed methods, at least for general purposes. It is however important to provide an explanation in cases where no compatibility is found. Discrepancies may arise due to variations in the parameters used for the Haser model. Firstly, the usage of the g-factors from Schleicher (2010). Those are anyway the most recent and complete tabulated values for the CN and they are largely used in recent publications,

as the ones used for comparison. Then, typically different authors refer to different sets of scale lengths, or calculate them by themselves (Cochran, 1985). Using a different set of scale lengths may cause variations to the result up to a factor of 3 (Fink and Combi, 2004). However, according to Cochran et al. (2012), the scale lengths can be considered, in first approximation, fully determined by the insolation and the heliocentric distance.

On the other side, different observational conditions may be several and often not quantifiable. Briefly, these are:

- Presence of clouds, resulting in a diminishing of the observed flux from both the source and the standard star used for flux calibration

- Variation in the illumination of the active area: if during different observations, the main active area of the comet is subject to a different illumination, for example, because it crosses the terminator line, the resulting production rate of the CN could be affected

- Different orientation of the slit: if the slit does not include an outgassing region, which instead is included in different observations, the production rate could change considerably

- Rotation of the comet: if the comet has for example a fast rotation, the illumination may be subject to sudden variations or periodicity

Furthermore, in his work on comet 1P/Halley during its 1985-86 perihelion, Fink (1994) reported small-scale inhomogeneities in the production rate of various gases. These day-to-day fluctuations were around 20% to 30%, which is higher than Fink's stated accuracy of at least 10% for his flux measurements. The fluctuations may be attributed to changes in the comet's activity or inhomogeneity in the outgassing. However, it should be noted that such variations can widely differ from one comet to another. His results suggest that comets' behavior can be unpredictable due to their intrinsic variability.

4.1.2   CN Production Rate vs Heliocentric Distance

The visualization of the CN production rate as a function of the heliocentric distance allows us to investigate if different dynamical groups follow different distributions and if the Q(CN) follows a peculiar general trend with heliocentric distance. Our results tend to suggest some grouping:
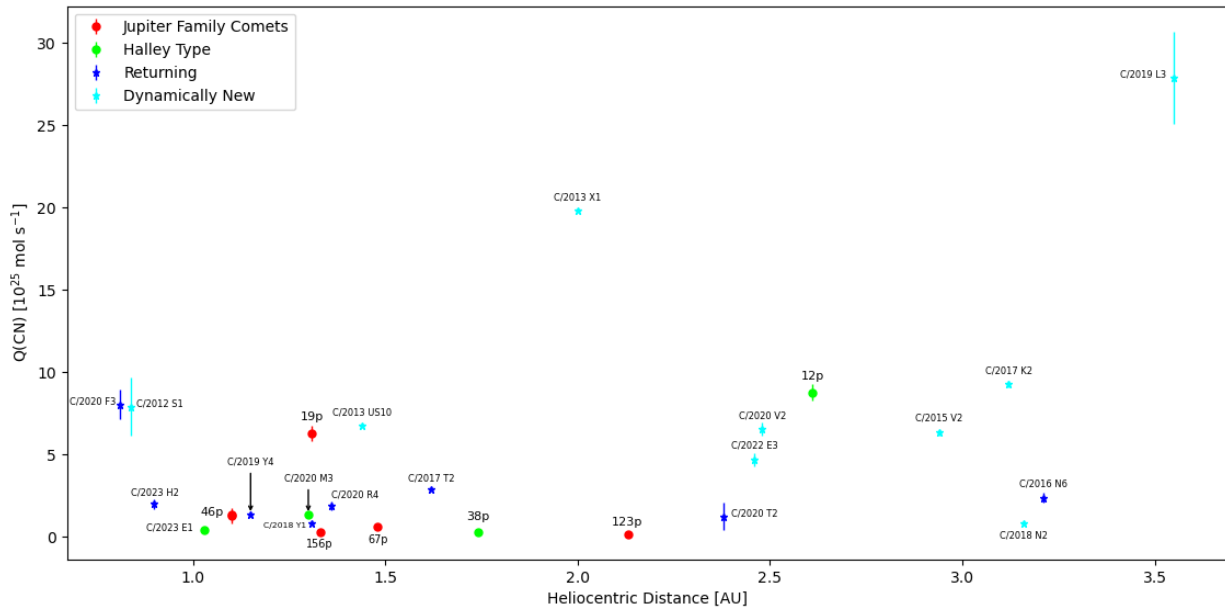
Figure 4.3: *The full dataset is represented in the plane Q(CN) vs r.*

Jupiter Family comets lie in the region of low Q(CN), indicating that their ice reservoirs may be running low due to their repetitive passages near the Sun. However, there is an exception to this trend, which is comet 19P Borrely which assumes relatively high values of Q(CN). This is a peculiar comet, with an asymmetric coma shape, and a noticeable jet located in a polar position. According to Yelle et al. (2004), this may be due to highly accelerated gas from a subsurface cavity that is emitted through a small aperture on the surface. This constant peculiar activity of the comet may explain the high activity value measured. However, if we look at 19P in the residual plot in Fig. 4.2 we find very good agreement with published values, confirming the intrinsic nature of this high activity.

Halley-Type comets follow the same trend, with values typically below 10^{25} mol s^{-1}, most likely for the same reason as Jupiter Family comets. Here detaches comet 12P Pons-Brooks, more deeply discussed ahead (Section 4.2.2). Returning and Dynamically New comets adjust on more high values of Q(CN), beyond 10^{26} mol s^{-1}. The higher values are reached by Dynamically New comets, which are thought to have the most pristine and abundant reservoirs of ice, being at their first (and only) crossing of the internal Solar System, as far as their orbital reconstruction can be achieved.

4.2   Specific Comets Investigation

For comets C/2023 H2, C/2023 E1 and 12P, whose observations covered my internship period, a deeper analysis was performed, by looking for trends in the variation of Q(CN) with the heliocentric distance.

4.2.1 C/2023 E1 ATLAS

E1 ATLAS is a Halley Type comet with a period of 85 years. It was discovered on March 1, 2023, by the NASA-funded Asteroid Terrestrial-impact Last Alert System. It reached the perihelion on 2023-07-01. For this comet is available one pre-perihelion observation, while all the others are post-perihelion. In Fig. 4.4 is reported the distribution of the CN production rate with varying heliocentric distance. It can be seen how the peak in the CN production rate is not reached at its perihelion but after ~ 0.2 AU. This comet, like others, shows asymmetrical gas production rates around perihelion (Rubin et al., 2014).

| Date | r | Q(CN) | Exptime | Slit |
yyyy-mm-dd	AU	10^{25} mol s^{-1}	s	μm
2023-06-25	1.03	3.98 ± 0.12	1200	150
2023-07-23	1.09	5.73 ± 0.50	900	200
2023-08-06	1.19	5.50 ± 0.61	300	200
2023-08-11	1.23	7.36 ± 0.40	600	200-600
2023-08-12	1.24	9.12 ± 1.06	300	200
2023-08-13	1.25	6.16 ± 0.54	300	200
2023-08-18	1.29	3.89 ± 0.15	1200	200-600

Table 4.3: *Observations program of comet C/2023 E1. The solar analog used for every night is 16 Cygni B, and the grating is the 300 lines/mm.*

These kinds of asymmetries are found also in the literature. A'Hearn et al. (1995) proposed a link between these asymmetries and the dynamical group, noting that Dynamically New comets tend to show a higher activity before perihelion, while no definite behaviour is seen for the other groups. For example, he found both 1P/Halley and 67P/C-G have a higher CN production after the perihelion. Since similar asymmetries in the activity are also found in dust production, the theory sustained by (Fray et al., 2004) on dust degradation as the principal source of CN seems to have some confirmations.

However, this aspect does not hold for every comet. Opitom et al. (2015b) found that in comet C/2013 R1 Lovejoy, the activity of dust has no similarities to that of CN, in its pre- and post-perihelion behaviour, suggesting the HCN in the nucleus may be the principal source of CN for this comet. The same author (Opitom et al., 2017), while studying the CN production rate during 67P perihelion in 2015 found out Q(CN) still increasing two weeks after perihelion. This trend in cometary activity has several proposed explanations. For example, this can be attributed to the accumulation of material in cold spots that starts to be illuminated only after perihelion (Rubin et al., 2014). Otherwise, it may be a change in the dust cross-section (Fulle et al., 2010), or internal changes due to the transition from amorphous to crystalline ice, coupled with different thicknesses of the irradiation dust mantle (Rosenberg and Prialnik, 2009).

4.2.2 Comet 12P Pons-Brooks

12P is one of the most interesting objects that crossed the sky in the last months. Observations of this comet date back to 1385 A.D., making it one of the oldest comets observed, second only to comet 1P Halley (Ye et al., 2020). It is classified as a Halley-type comet, belonging to the Neptune family, with a period of 71 years. This comet periodically undergoes so-called outburst events. From an observative point of view, an outburst is defined as a sudden increase in a comet's luminosity, between 2 to 5 magnitudes (Hughes, 1975) and are typically observed in periodic or
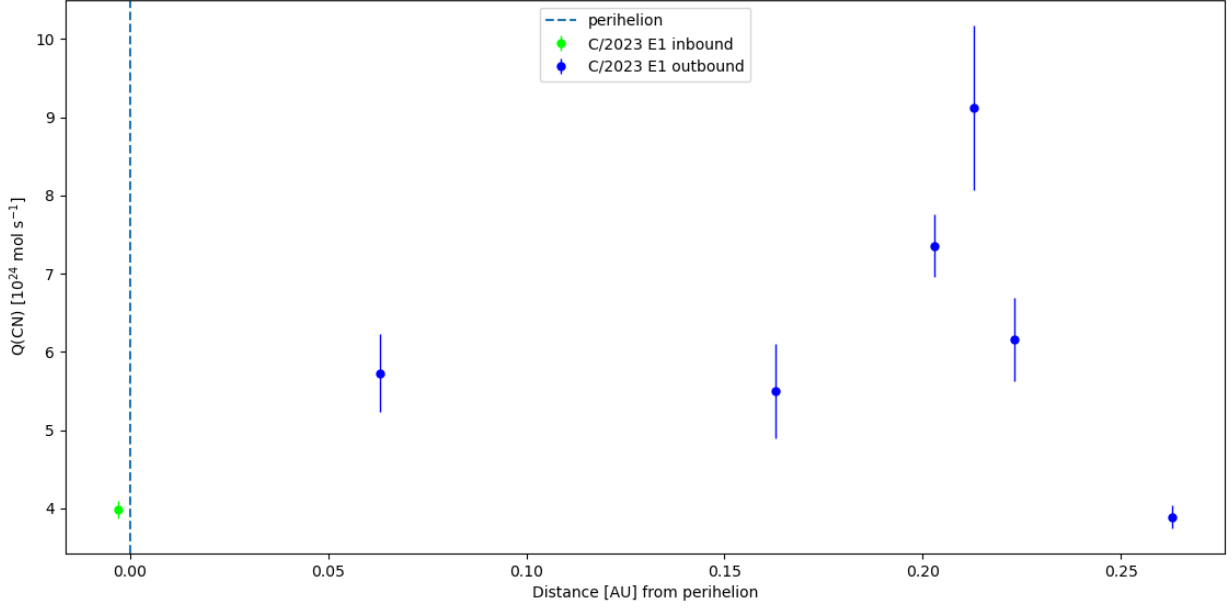
Figure 4.4: *CN production rate is plotted as a function of the heliocentric distance. The CN activity continues to increase after perihelion, to reach its maximum around 0.21 AU.)*

Date yyyy-mm-dd	r AU	Q(CN) 10^{25} mol s^{-1}	Exptime s	Slit μm
2023-07-23	3.85	2.56 ± 0.33	600	600
2023-08-11	3.65	2.54 ± 0.42	900	200-600
2023-08-21	3.55	3.50 ± 0.31	1800	200
2023-10-01	3.10	3.39 ± 0.58	600	150
2023-10-07	3.03	10.72 ± 0.43	300	200
2023-11-12	2.61	8.77 ± 0.47	600	150-300
2023-11-17	2.55	45.76 ± 1.16	300	200-400
2023-11-18	2.54	34.29 ± 0.92	180	200
2023-11-22	2.49	13.08 ± 0.85	30	150-300

Table 4.4: *Observative program for comet 12P. All the spectra were taken with the 300 lines/mm grating, with the exception of 17-11 and 18-11 nights for which the 1200 lines/mm grating was equipped.*

parabolic comets. Various physical explanations have been proposed, but the most accepted is the one proposed by Ipatov and A'Hearn (2010). This scenario suggests the presence of cavities below the surface of a cometary nucleus, filled with materials subject to very high gas pressure. The outburst is observed when the superficial layers right above these cavities are torn away from active outgassing.

Comet 12P underwent various documented outbursts, like those that occurred during the last two perihelion passages, on 1883-84 and 1953-54, in which the magnitude increased by a factor 3-4. At the time of this writing, 12P is approaching its 2024 perihelion, expected on April, 24. On its inbound orbit, the comet already experienced three outbursts: one on July, 19, and two more which are covered in the observations here presented, October, 5 (Usher et al., 2023) and November, 14 (Jehin et al., 2023a). By following the trend in the CN production rates, from July 23 to November 11, two peaks in Q(CN) can be observed in correspondence with the outbursts

(Fig. 4.5). In particular, the November outburst turned much more intense, with Q(CN) increasing of about one order of magnitude, while in October by a factor of 3.
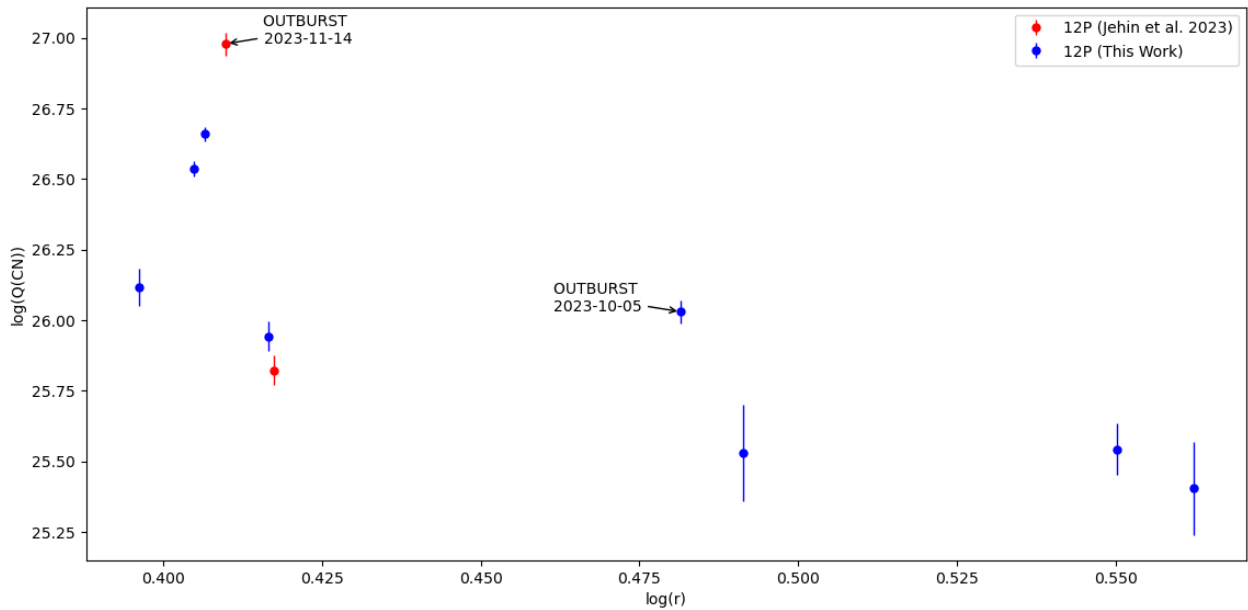
Figure 4.5: *Q(CN) as a function of the heliocentric distance. It is evident the peak of CN production in correspondence of the two documented outbursts of 2023-10-05 (Usher et al., 2023) and 2023-11-14 (Jehin et al., 2023a). To better observe the trend in Q(CN) two observations by Jehin et al. (2023a) have been added to ours.*

It is also interesting to visualize the variation that occurred in 12P's spectra before and after an outburst. Fig. 4.6 shows two spectra of comet 12P, the upper dates to 2023-10-07 and the lower to 2023-11-17. While the upper image is too rumorous to detect any significant emission other than CN band at 3880 Å, the situation is radically different in the second spectrum. Several lines belonging to the C_3 band, between 3920 and 4100 Å. Around 4200 Å is visible in the weak CN $\Delta\nu = -1$ band, and CN lines around 4300 Å. Finally, in the region between 4600 and 4740 Å lines from C_2 $\Delta\nu = 1$ are detected.
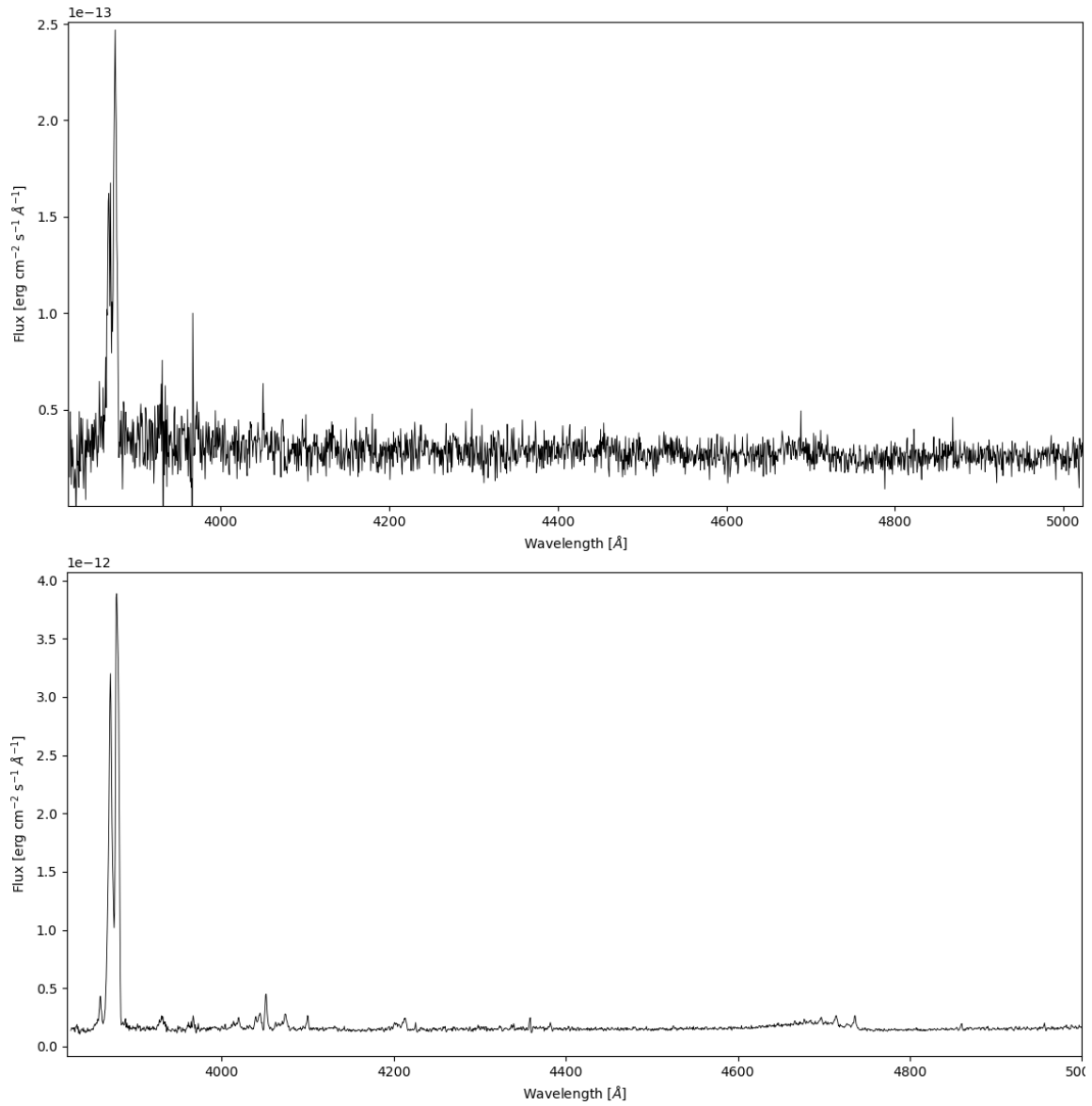
Figure 4.6: *Spectra of 12P taken with 1.22-m Galileo telescope. Both spectra have the same configuration, 1200 tr/mm grating and 200 µm wide slit and 300s of exposure. The upper image is from 2023-10-07 night, while the lower is taken on 2023-11-17.*

4.2.3 C/2023 H2 Lemmon

Comet Lemmon, categorized as a Returning comet, was first identified on April 23, 2023, through the Mount Lemmon Survey. Despite the relatively limited number of observations in its current observational program (see Table 4.5), it holds particular significance due to its coverage of two pre-perihelion and three post-perihelion dates. The Q(CN) vs r plot for Comet Lemmon is depicted in Figure 4.7. Notably, the CN production rate trend exhibits similarities to the behavior observed in comet E1, specifically, an asymmetry pre/post perihelion. However, in this case, with a more balanced distribution of observations around perihelion, an additional asymmetry becomes apparent. The increase in Q(CN) pre-perihelion differs from the rate of decrease post-perihelion. It is noteworthy to mention that this second type of asymmetry aligns with findings presented by Opitom et al. (2015b) on comet 67P.

| Date | r | Q(CN) | Exptime | Slit |
yyyy-mm-dd	AU	10^{25} mol s^{-1}	s	μm
2023-10-12	0.95	0.96 ± 0.06	600	150
2023-10-25	0.90	2.08 ± 0.05	900	150-300-600
2023-11-12	0.93	1.04 ± 0.04	60	150-300-600
2023-11-17	0.96	0.70 ± 0.03	120	200-400-600

Table 4.5: *Observative program for comet C/2023 H2. All the spectra were taken with the 300 lines/mm grating.*
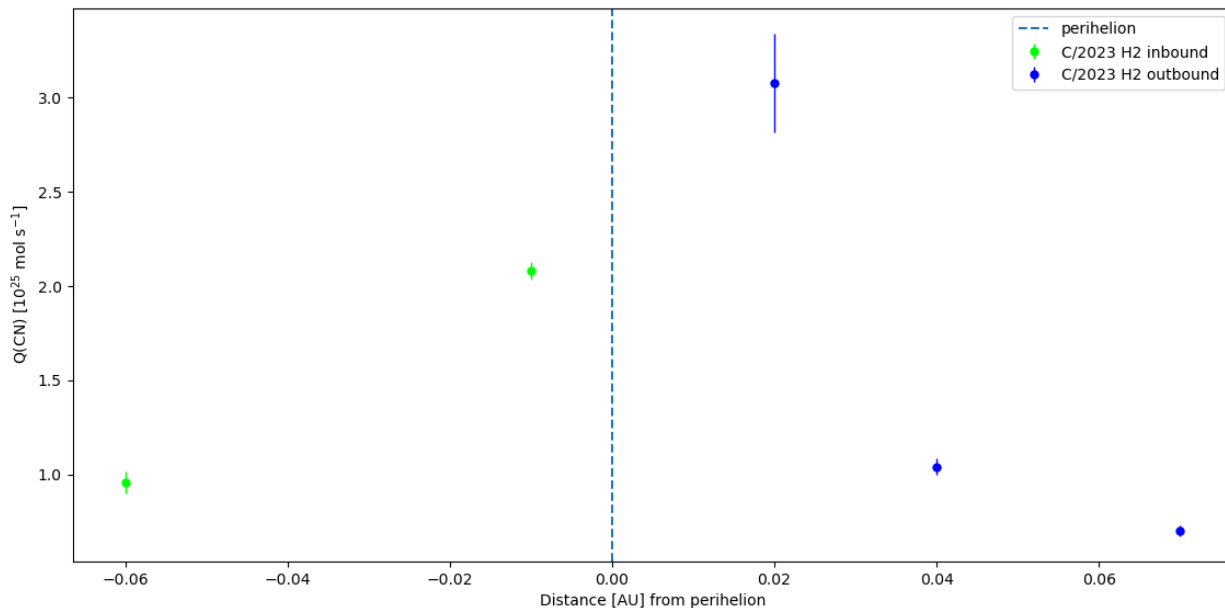
Figure 4.7: *Q(CN) as a function of the heliocentric distance. The asymmetry both in the intensity and slope of the Q(CN) before and after perihelion is visible.*

Chapter 5

Conclusions

In this thesis, I conducted an extensive investigation into the spectroscopic analysis of comets observed with the 1.22m Galileo telescope at the Asiago Observatory. The primary focus was on three specific comets, the Halley Type C/2023 E1, the Returning C/2023 H2 and the outbursting Halley Type 12P. In addition to being directly involved in the observation of these objects, I also reduced the collected spectra and developed a Python code for the computation of the CN violet system production rates within the framework of a simplified Haser model, providing insights into their activity.

As part of my research, I extended this analysis to include the entire sample of comets from the Asiago Atlas project. While I did not personally reduce this broader dataset, I sought an alternative approach to compute their CN production rate. I discovered that a literature-derived version of the standard Haser model proved effective for handling older data. The comparison of production rates derived from this method with existing literature demonstrated a good agreement, affirming the reliability of the adopted Haser model.

Through the investigation of CN production rates, it was highlighted a correlation between the dynamical type of comets and how they are distributed on the production rate vs. heliocentric distance plane. This finding helps to broaden our understanding of the various behaviours exhibited by comets as they travel towards the Sun.
Noticeable patterns emerged from the detailed follow-up analysis of the comets which I directly observed, C/2023 E1, C/2023 H2, and 12P. For comet C/2023 E1, an asymmetry in production rate concerning perihelion was unveiled, with the maximum rate occurring post-perihelion. Similarly, comet C/2023 H2 exhibited this asymmetry, with the additional detail of different increasing/decreasing slopes before and after perihelion. Notably, comet 12P displayed clear signatures of recurring outbursts in its CN production rate, manifesting as distinct peaks corresponding to each outburst event.

In conclusion, the spectroscopic analysis of comets, as observed through the 1.22m Galileo telescope, has shown that even one-meter-class instruments can make significant scientific contributions. This study highlights the importance of continuous monitoring and establishes the Galileo telescope as a valuable tool for cometary observations as it offers a promising platform for future cometary research.

In the prospect of future developments, my work sows the seeds for the potential utilization of more advanced approaches such as Festou's vectorial model for the investigation of the CN production rate. Moreover, production rates for other visible optical bands like C_2 and C_3 may be

computed, allowing for their comparison with CN production rates. By prolonging the cometary follow-up, we could acquire additional data points for an enhanced dataset, contributing to the refinement of existing results and providing a more comprehensive understanding of cometary behaviour.

Appendix A
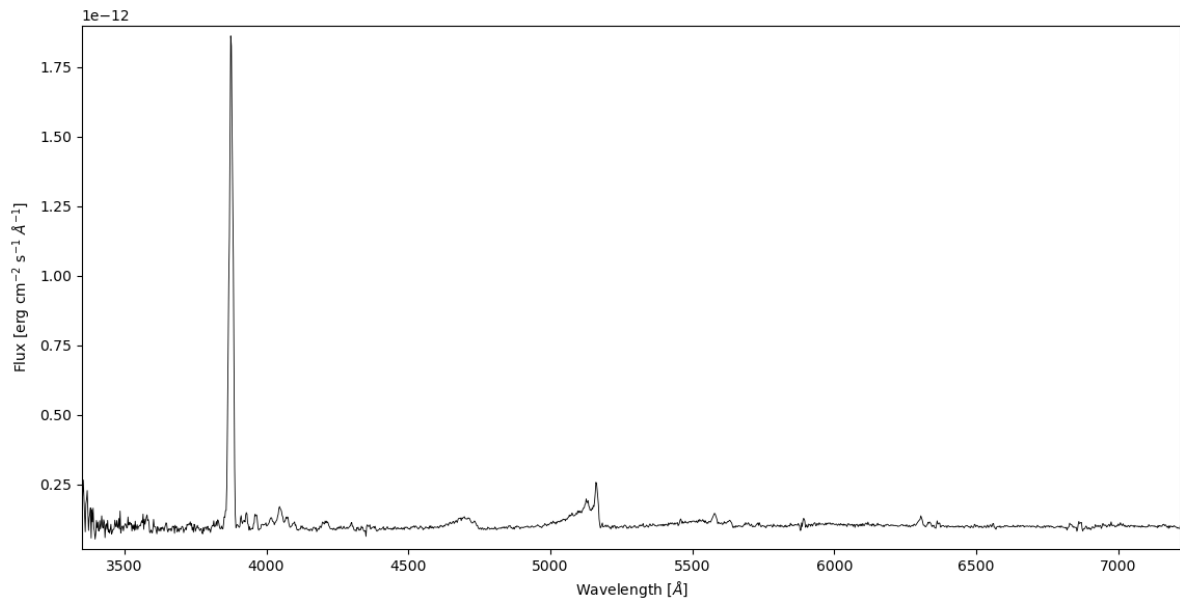
Asiago Atlas of Comets - Complete Spectral Dataset

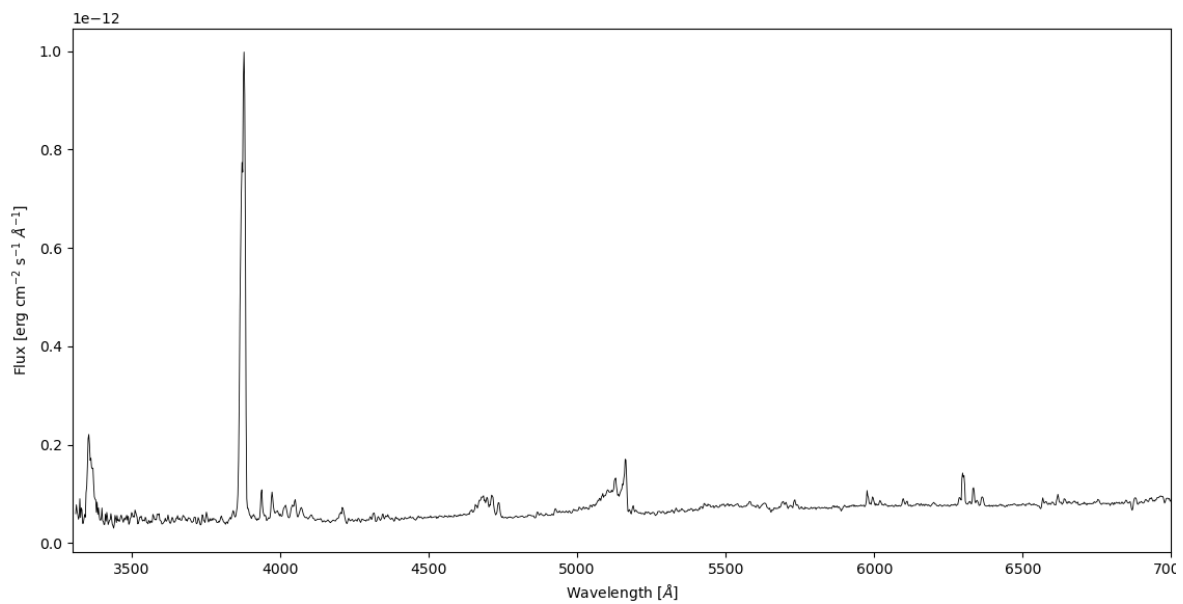Figure A.1: *12P 2023-12-03. 300 lines/mm grating, 300 μm slit width.*
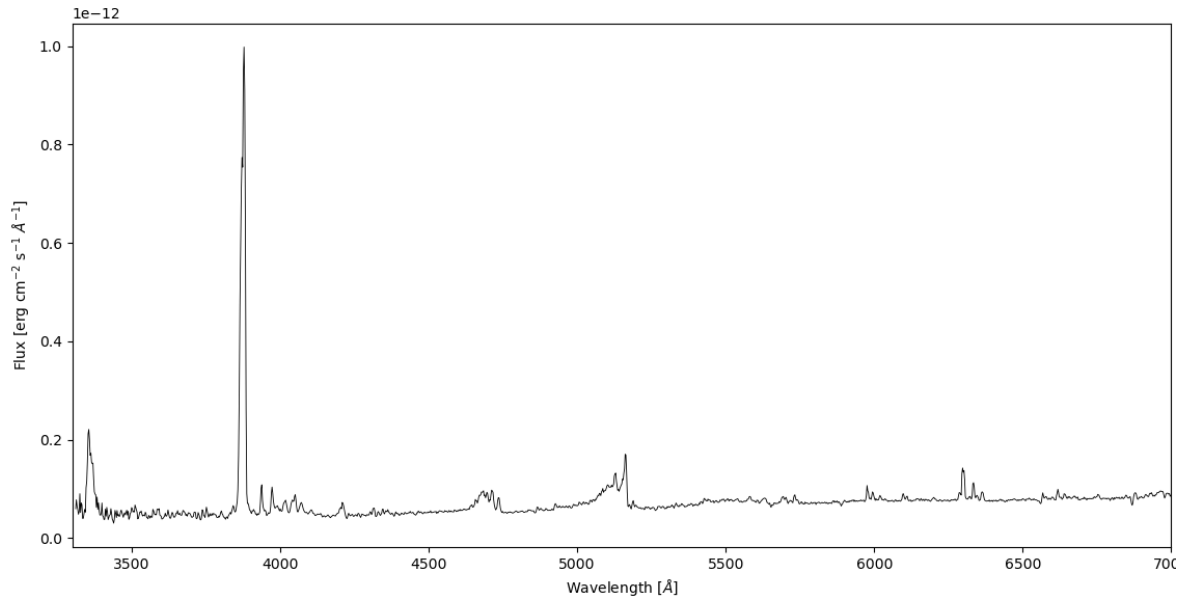

Figure A.2: *19P 2022-01-13. 300 lines/mm grating, 200 μm slit width.*
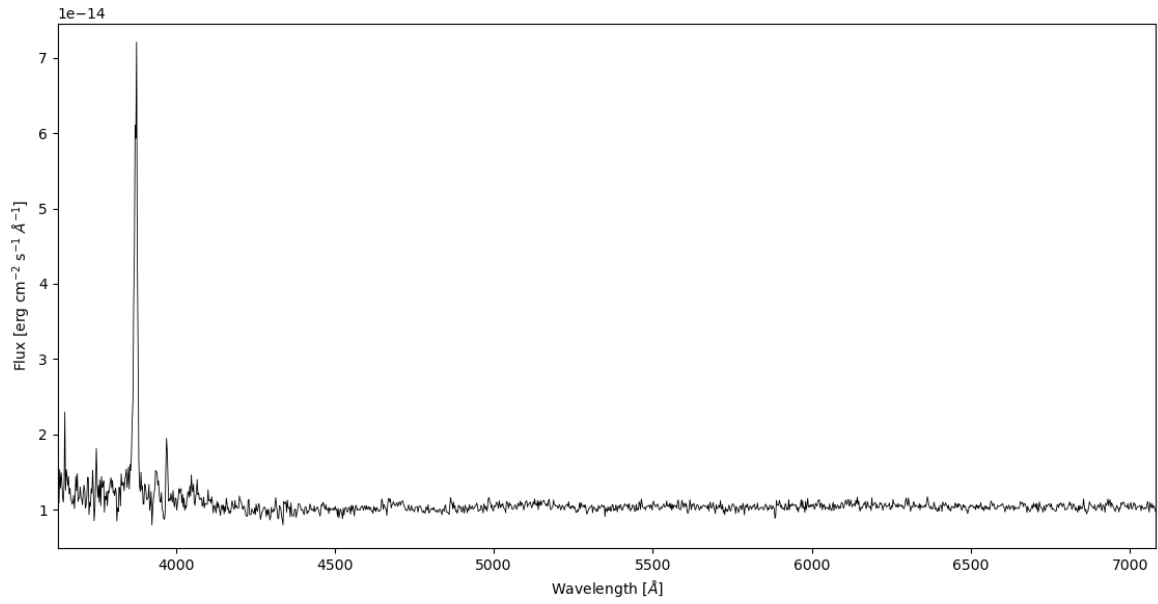
Figure A.3: *19P 2022-01-13. 300 lines/mm grating, 200 μm slit width.*
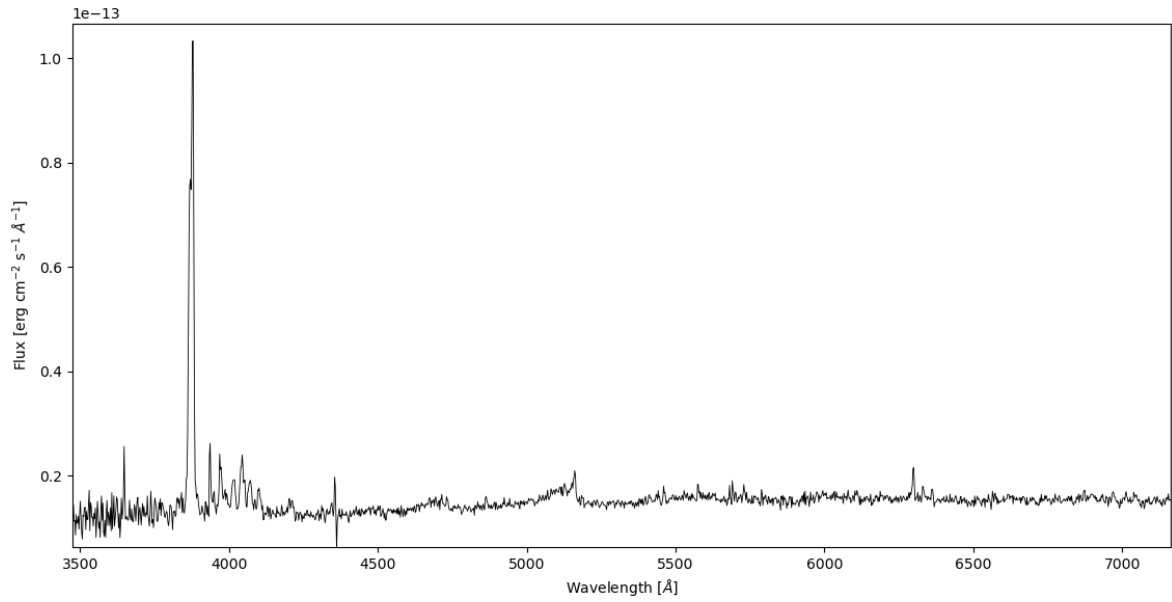
Figure A.4: *38P 2019-01-05. 300 lines/mm grating, 200 μm slit width.*
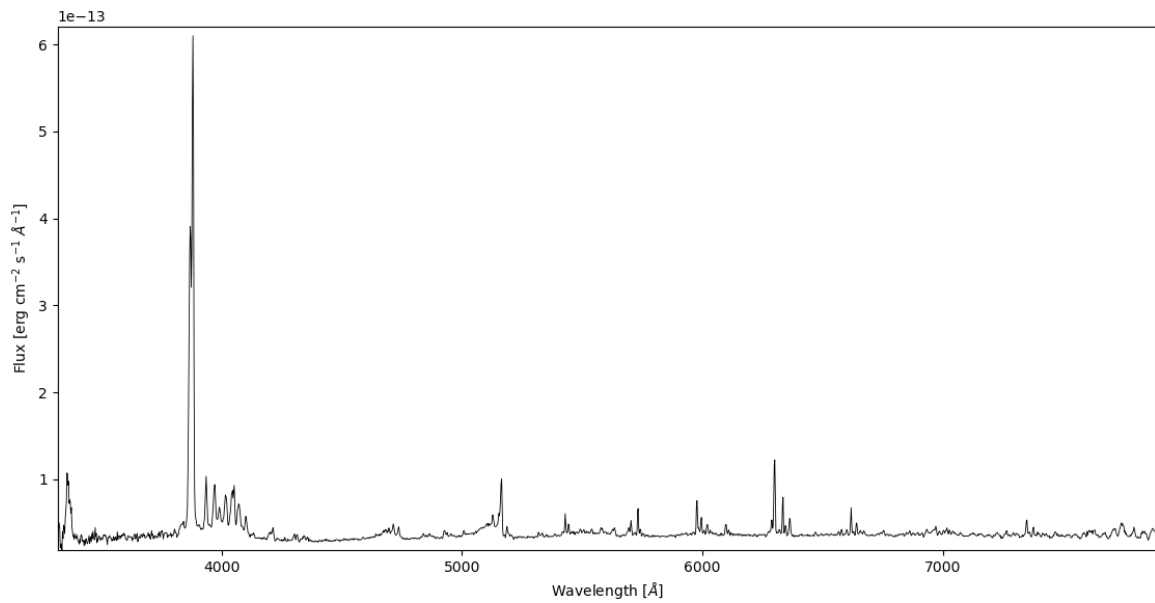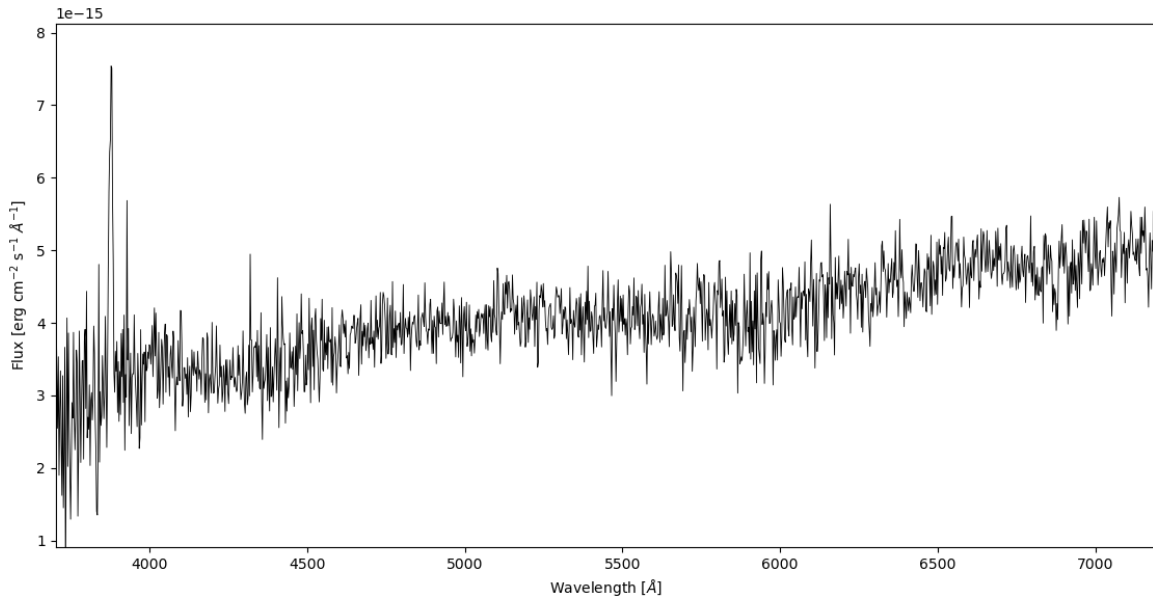

Figure A.5: *46P 2019-01-06. 300 lines/mm grating, 200 μm slit width.*
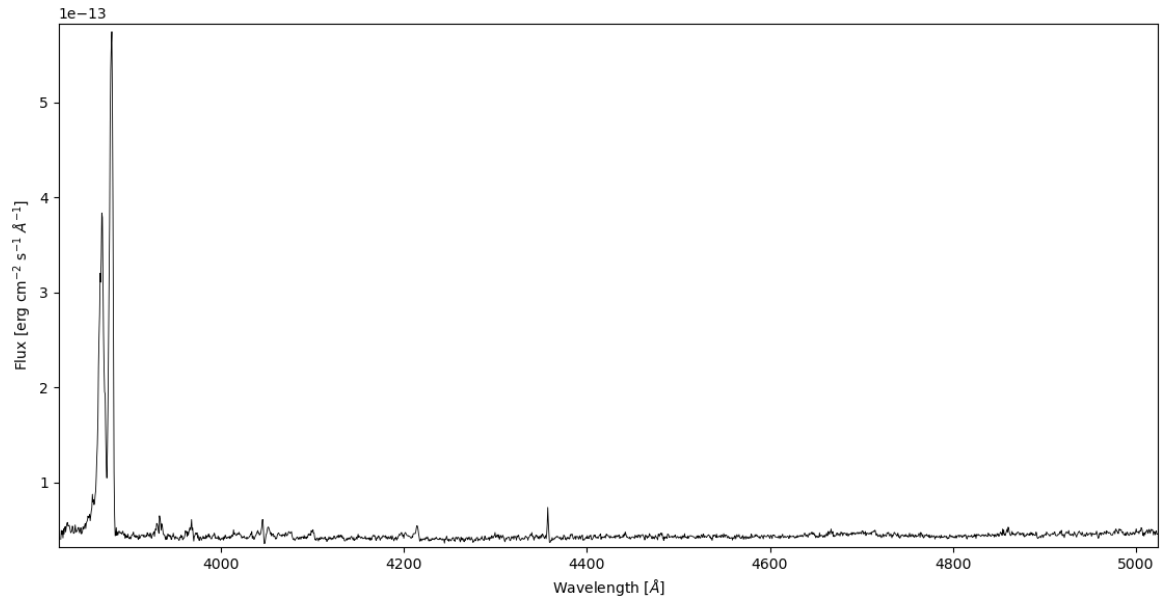
Figure A.6: *67P 2022-01-11. 1200 lines/mm grating, 200 μm slit width.*
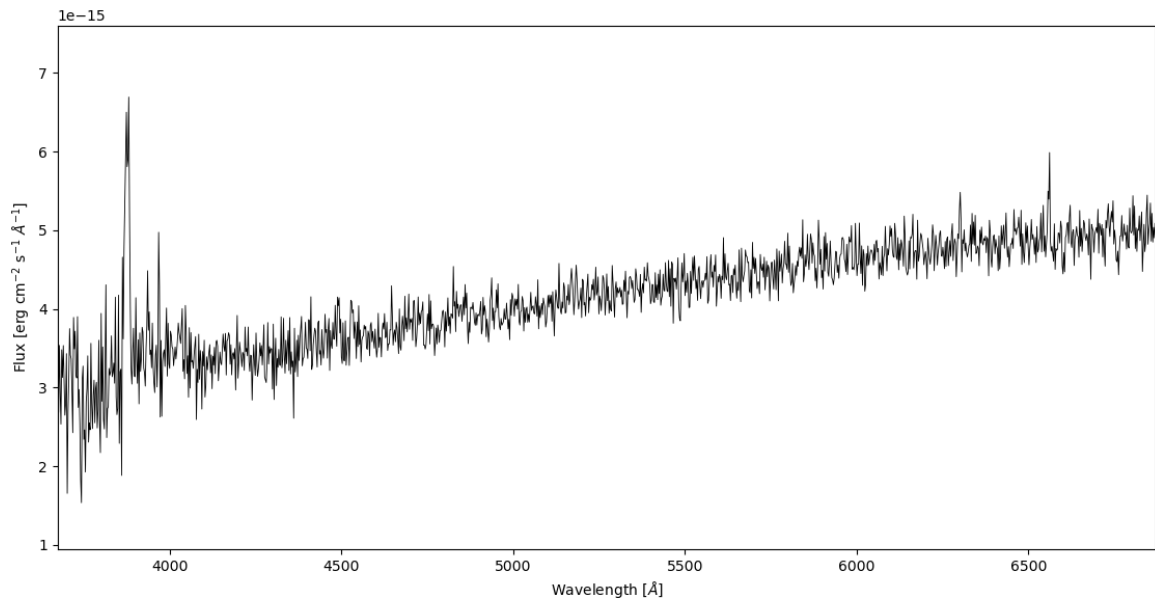
Figure A.7: *123P 2019-02-17. 300 lines/mm grating, 250 μm slit width.*
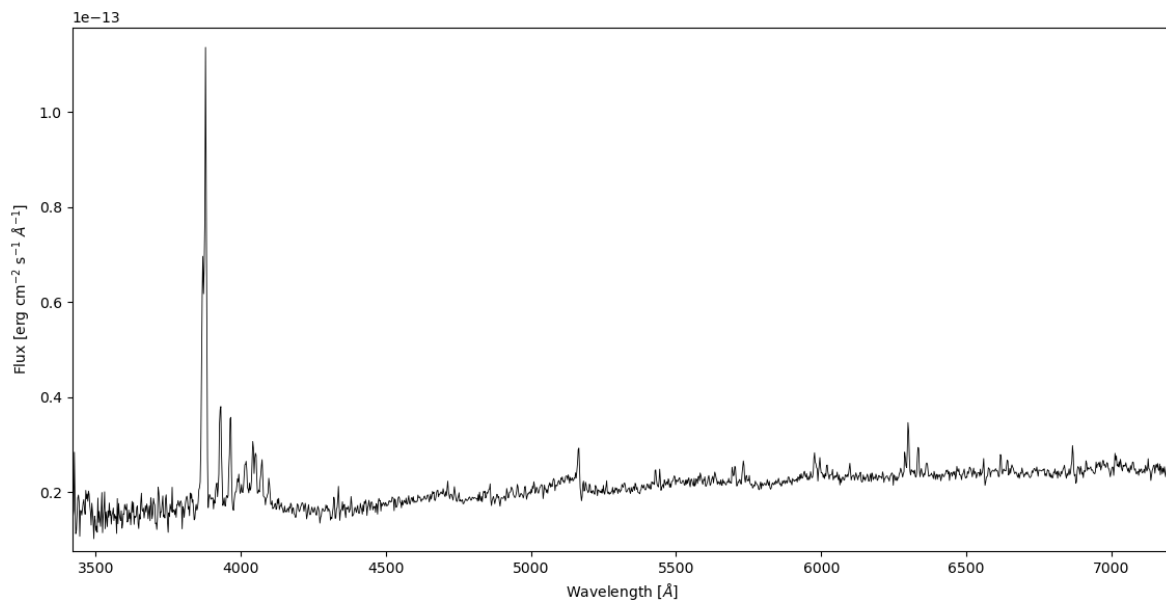
Figure A.8: *156P 2020-01-13. 300 lines/mm grating, 200 μm slit width.*
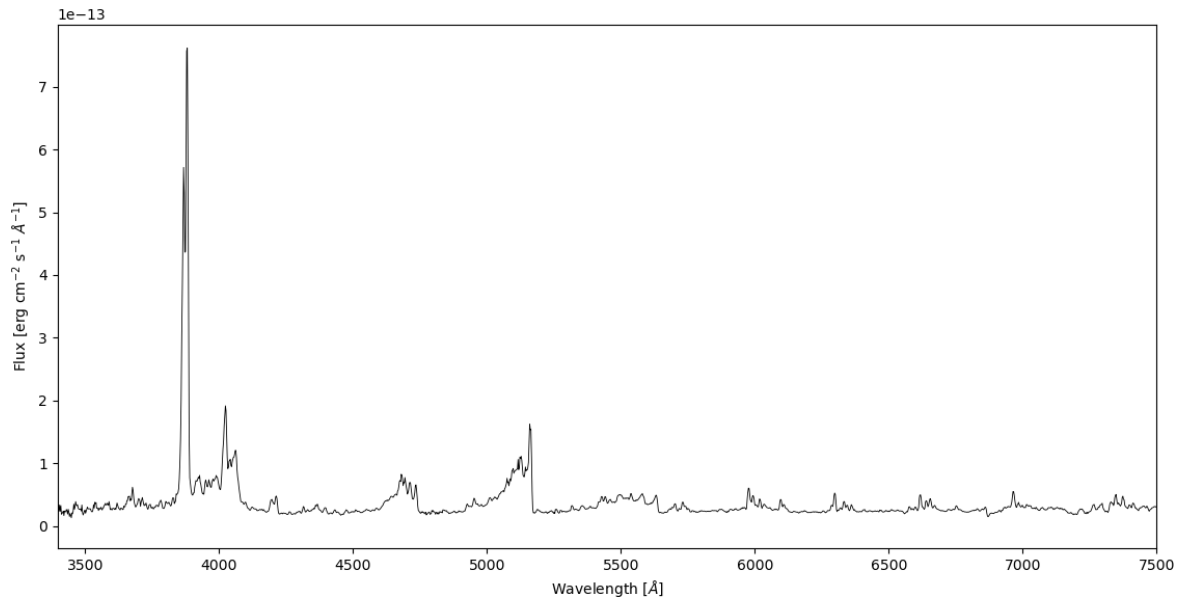
Figure A.9: *C/2012 S1 2013-11-07. 300 lines/mm grating, 250 μm slit width.*
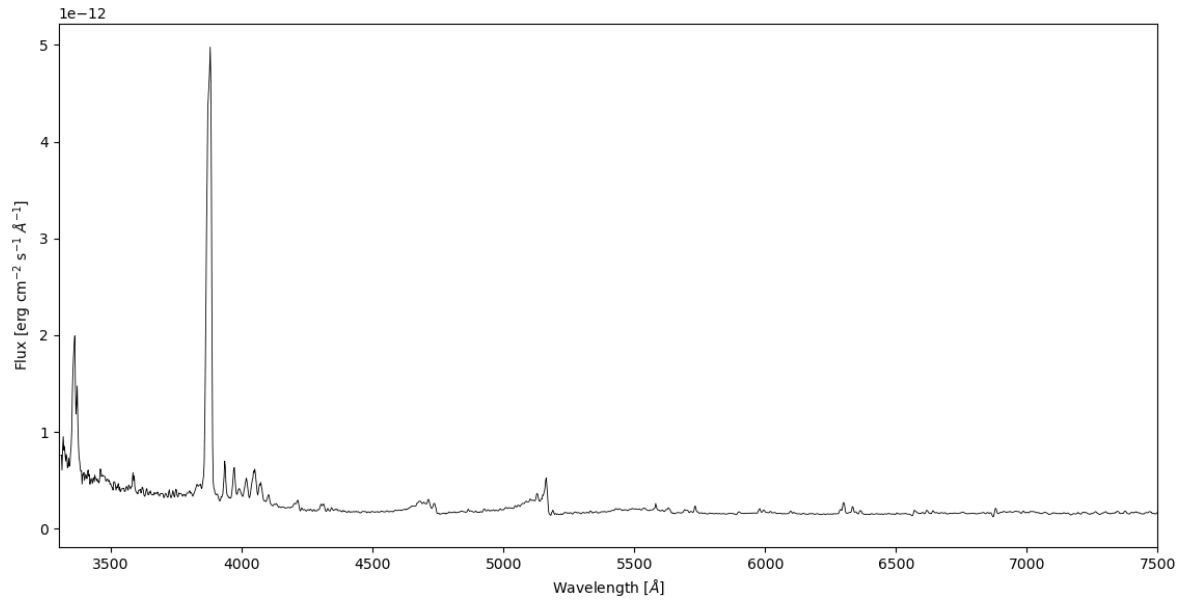
Figure A.10: *C/2013 US10 2016-01-21. 300 lines/mm grating, 200 μm slit width.*
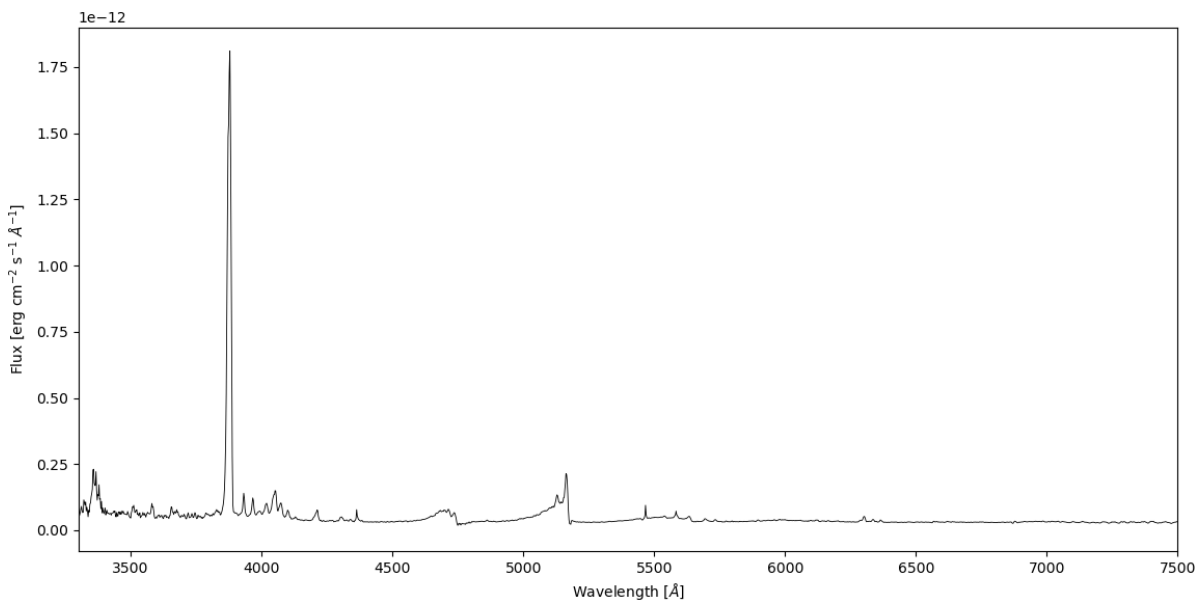
Figure A.11: *C/2013 X1 2016-01-06. 300 lines/mm grating, 200 μm slit width.*

Figure A.12: *C/2015 V2 2016-11-30. 300 lines/mm grating, 200 μm slit width.*

Figure A.13: *C/2016 N6 2023-01-06. 300 lines/mm grating, 200 μm slit width.*
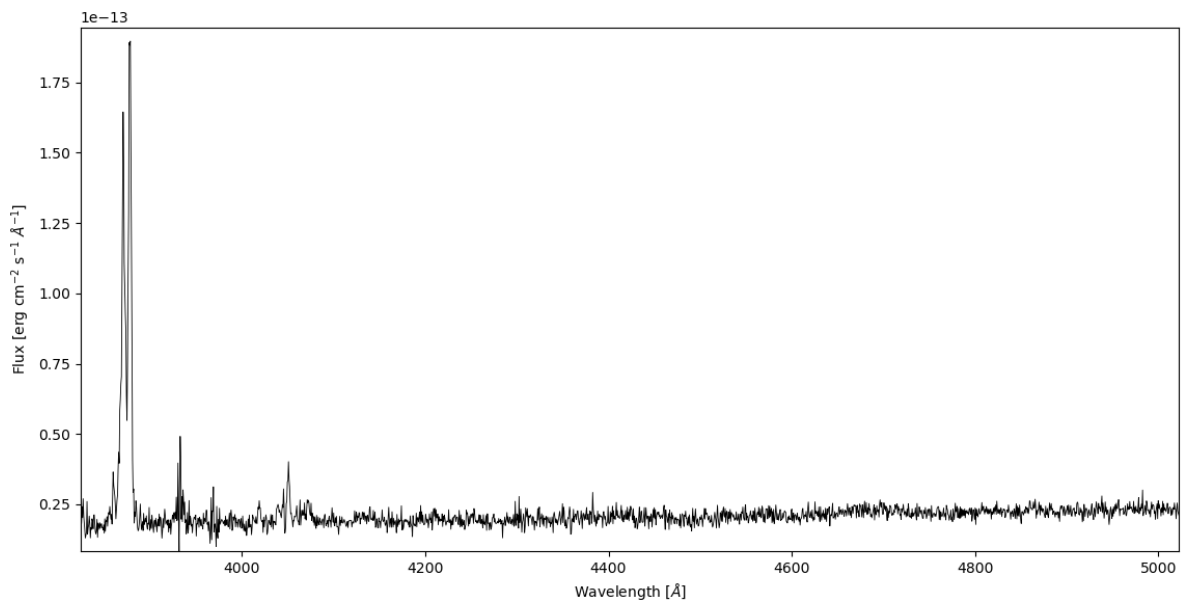

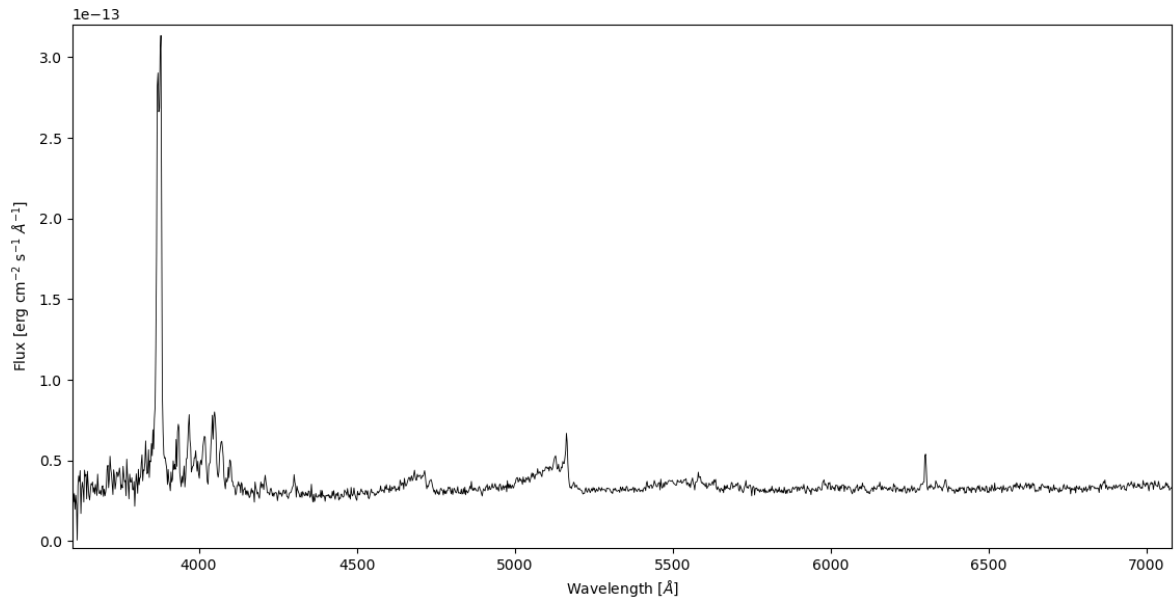Figure A.14: *C/2017 K2 2022-05-21. 1200 lines/mm grating, 200 μm slit width.*

Figure A.15: *C/2017 T2 2020-05-02. 300 lines/mm grating, 250 µm slit width.*

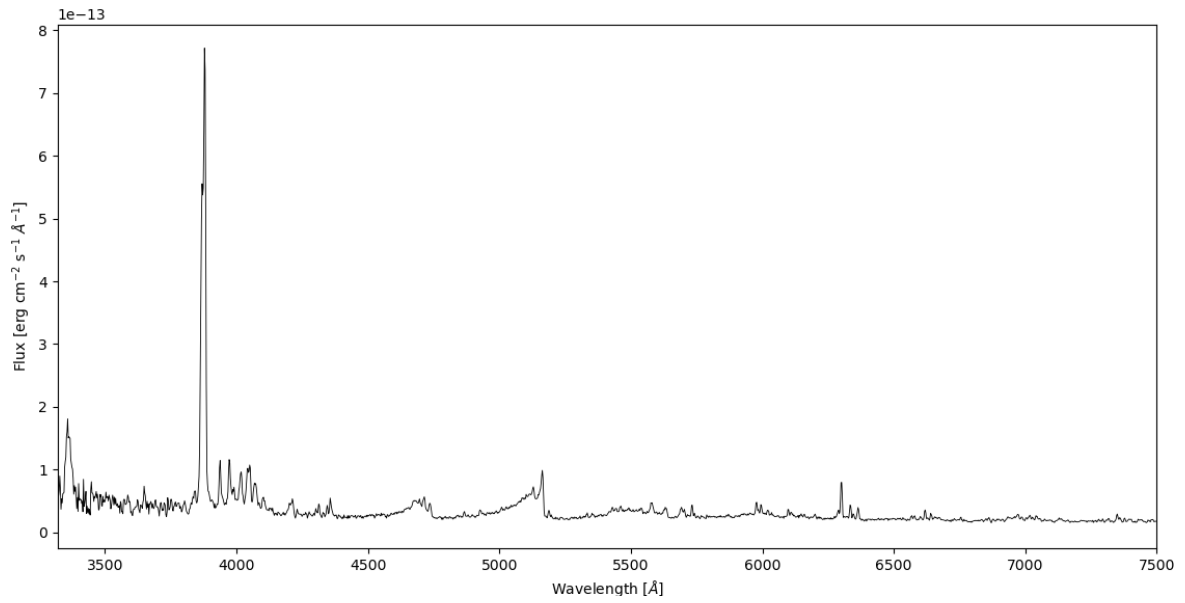

Figure A.16: *C/2018 Y1 2019-02-21. 300 lines/mm grating, 200 µm slit width.*
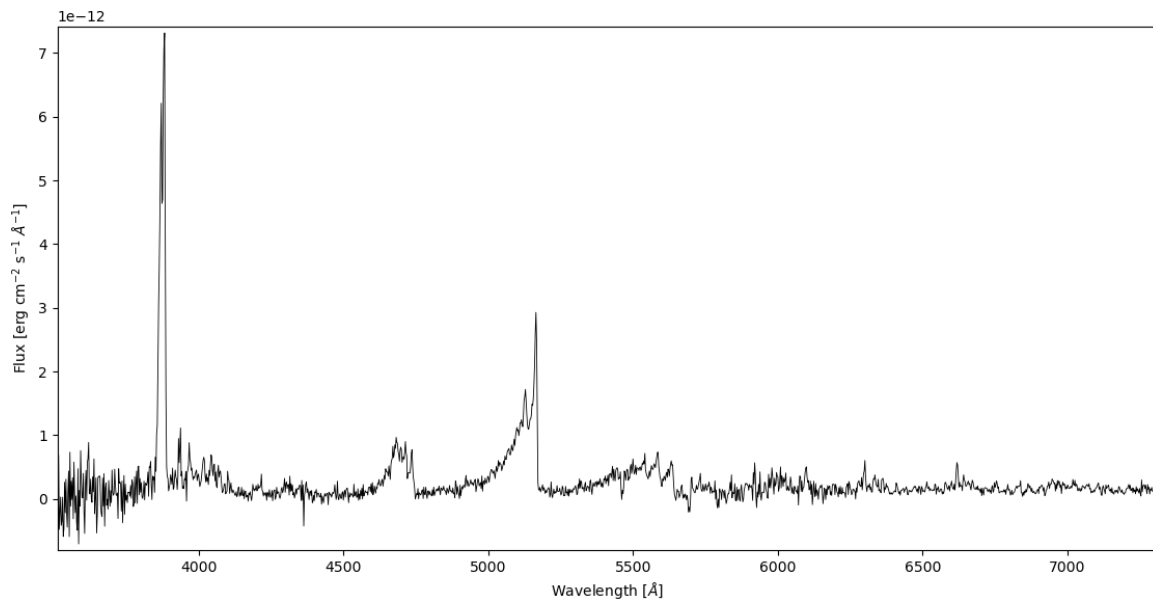

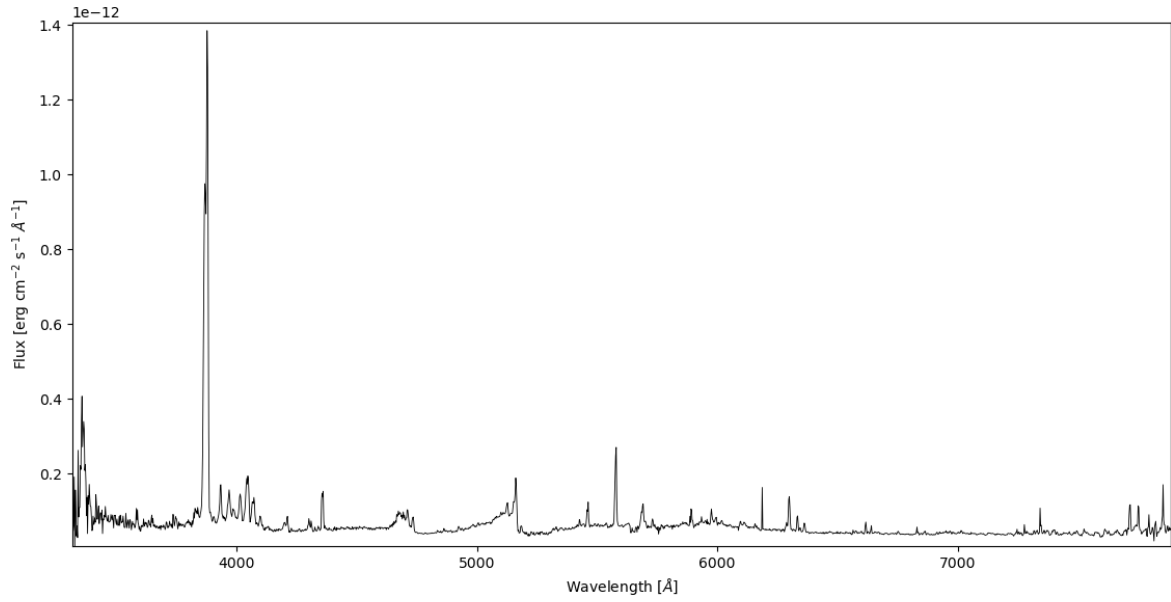Figure A.17: *C/2020 F3 2020-07-30. 300 lines/mm grating, 200 µm slit width.*

Figure A.18: *C/2020 M3 2020-11-13. 300 lines/mm grating, 222 μm slit width.*

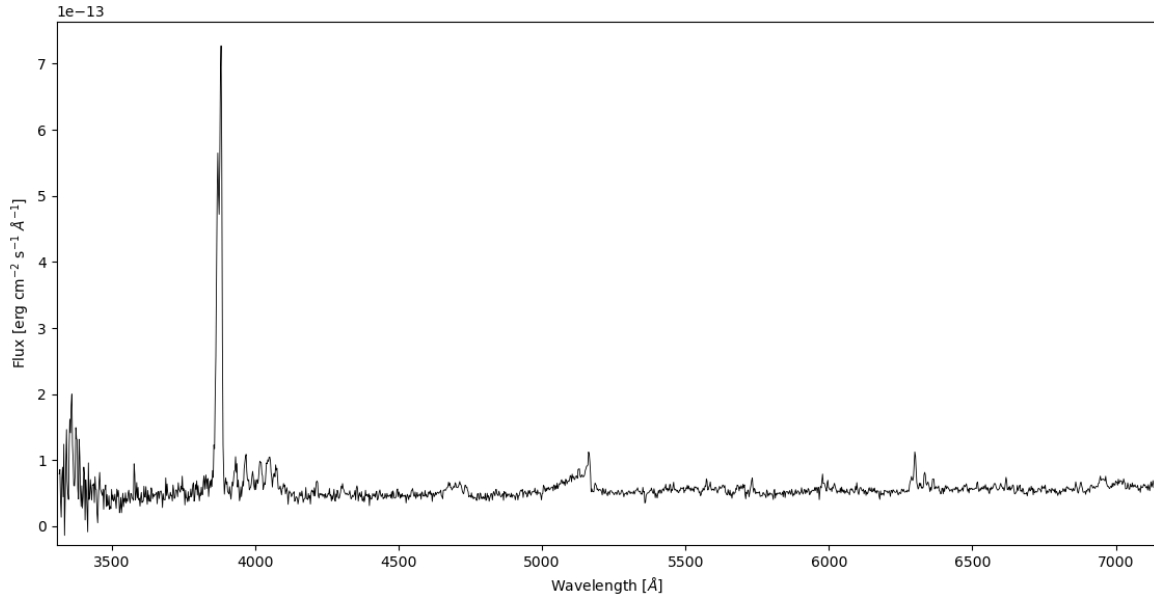Figure A.19: *C/2020 R4 2021-04-25. 300 lines/mm grating, 200 μm slit width.*
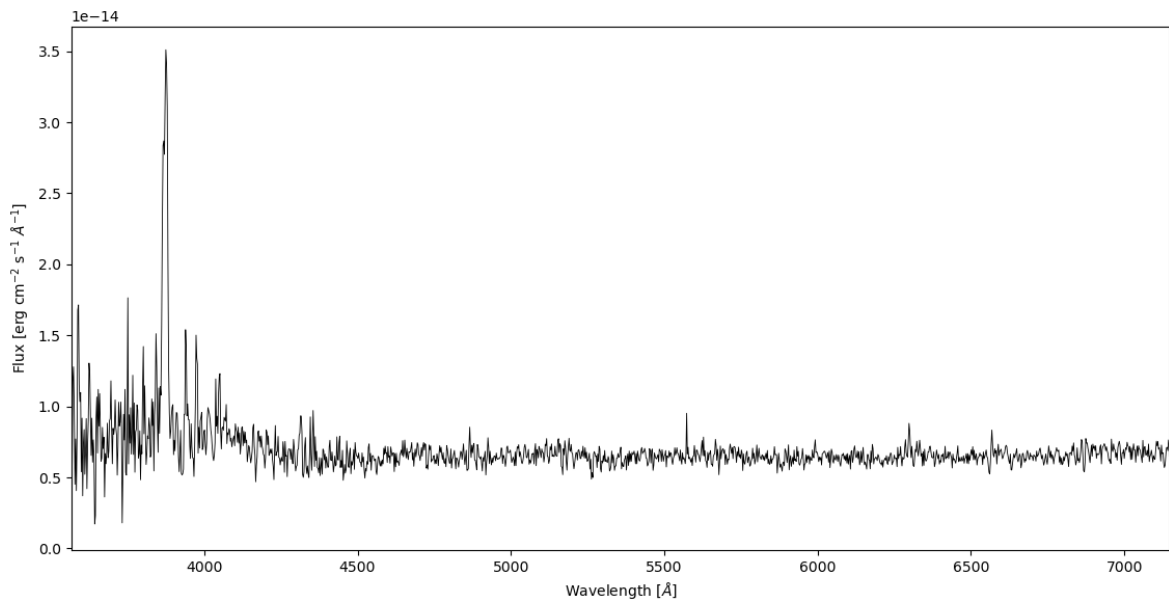

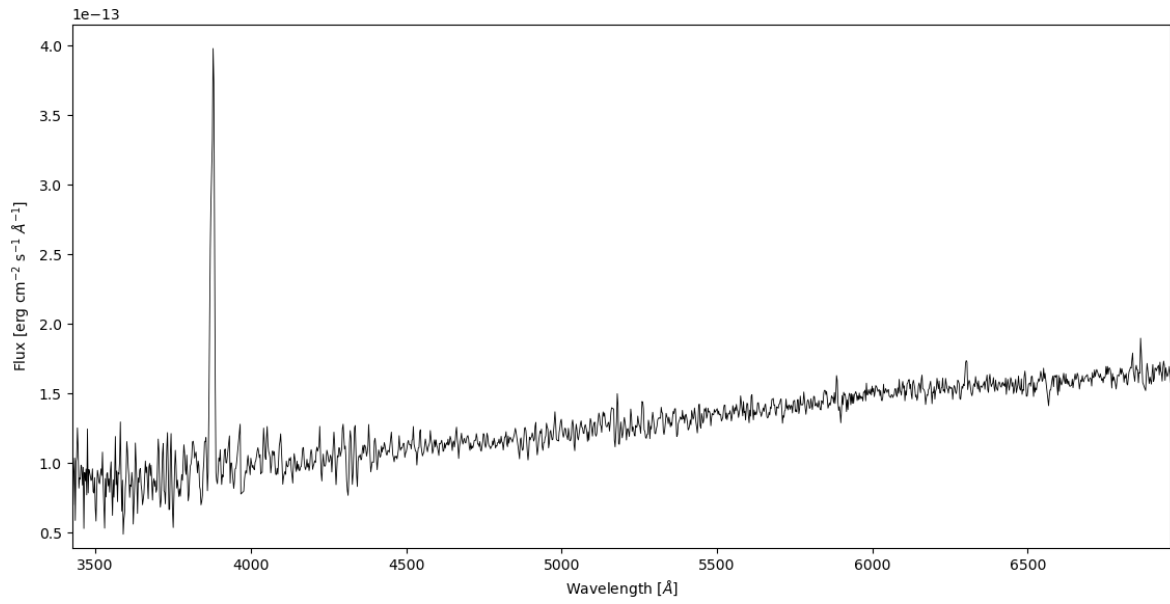Figure A.20: *C/2020 T2 2021-03-31. 300 lines/mm grating, 200 μm slit width.*

Figure A.21: *C/2022 E3 2022-08-22. 300 lines/mm grating, 200 μm slit width.*

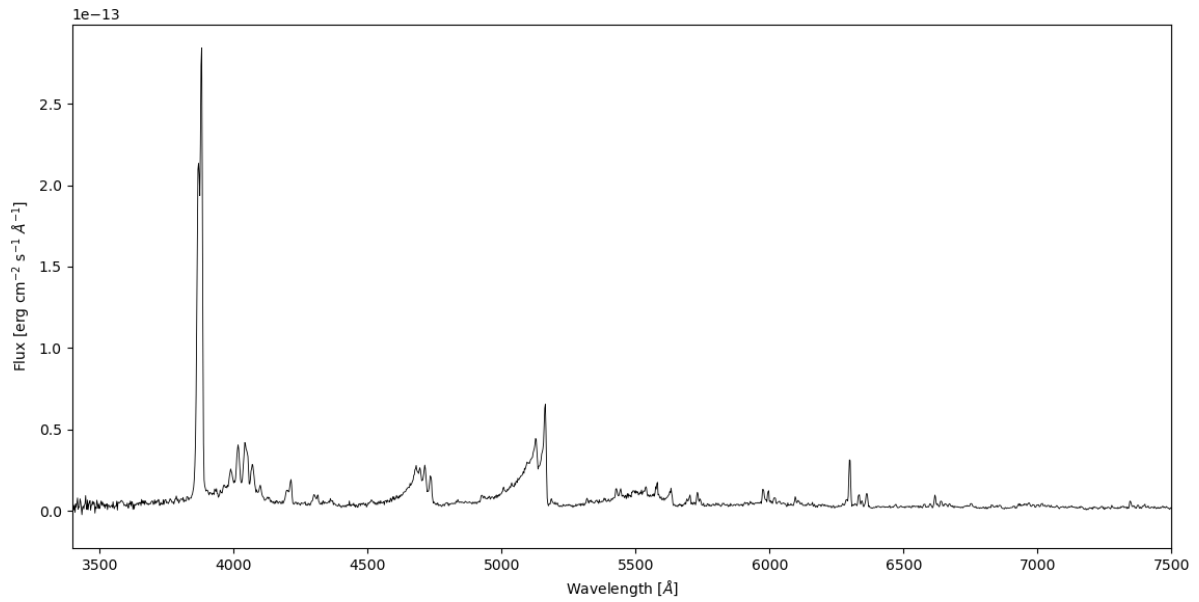
Figure A.22: *C/2023 E1 2023-08-18. 300 lines/mm grating, 200 μm slit width.*
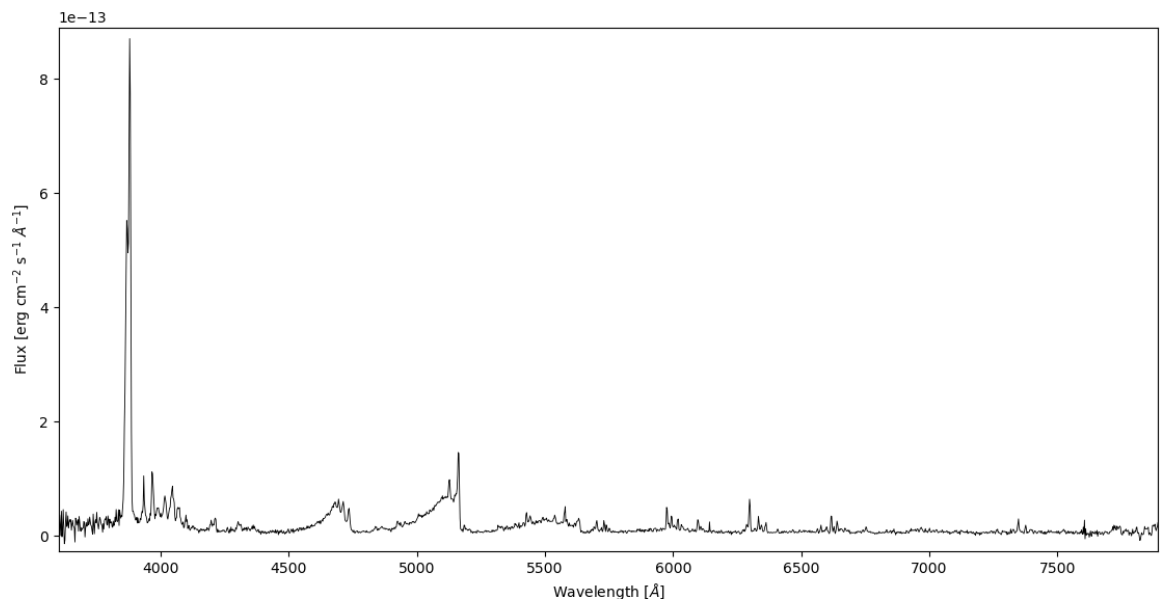

Figure A.23: *C/2023 H2 20231025. 300 lines/mm grating, 150 μm slit width.*

Bibliography

A'Hearn, M. F. (1982). Spectrophotometry of comets. In *Comets*. University of Arizona Press Tucson, Arizona.

A'Hearn, M. F., Millis, R. C., Schleicher, D. G., Osip, D. J., and Birch, P. V. (1995). The ensemble properties of comets: Results from narrowband photometry of 85 comets, 1976-1992. *Icarus*, 118(2):223–270.

A'Hearn, M. F. and Millis, R. L. (1980). Abundance correlations among comets. , 85:1528–1537.

Arpigny, C. (1964). Detailed study of the CN violet (0, 0) band in cometary spectra. *Annales d'Astrophysique*, 27:393.

A'Hearn, M. F., Belton, M. J. S., Delamere, W. A., Feaga, L. M., Hampton, D., Kissel, J., Klaasen, K. P., McFadden, L. A., Meech, K. J., Melosh, H. J., Schultz, P. H., Sunshine, J. M., Thomas, P. C., Veverka, J., Wellnitz, D. D., Yeomans, D. K., Besse, S., Bodewits, D., Bowling, T. J., Carcich, B. T., Collins, S. M., Farnham, T. L., Groussin, O., Hermalyn, B., Kelley, M. S., Kelley, M. S., Li, J.-Y., Lindler, D. J., Lisse, C. M., McLaughlin, S. A., Merlin, F., Protopapa, S., Richardson, J. E., and Williams, J. L. (2011). Epoxi at comet hartley 2. *Science*, 332(6036):1396–1400.

Bockelée-Morvan, D. and Biver, N. (2017). The composition of cometary ices. *Phil. Trans. R. Soc.*

Bockelée-Morvan, D., Crovisier, J., Mumma, M., and Weaver, H. (2004). The composition of cometary volatiles. *Comets II.*

Boehnhardt, H., Delahodde, C., Sekiguchi, T., Tozzi, G., Amestica, R., Hainaut, O., Spyromilio, J., Tarenghi, M., West, R., Schulz, R., and Schwehm, G. (2002). Vlt observations of comet 46p/wirtanen. *Astronomy Astrophysics - ASTRON ASTROPHYS*, 387:1107–1113.

Boice, D. C., Britt, D. T., Nelson, R. M., Sandel, B. R., Soderblom, L. A., Thomas, N., and Yelle, R. V. (2002). The Near-Nucleus Environment of 19P/Borrelly During the Deep Space One Encounter. In *Lunar and Planetary Science Conference*, Lunar and Planetary Science Conference, page 1810.

Cambianica, P., Cremonese, G., Munaretto, G., Capria, M. T., Fulle, M., Boschin, W., Di Fabrizio, L., and Harutyunyan, A. (2021). A high-spectral-resolution catalog of emission lines in the visible spectrum of comet C/2020 F3 (NEOWISE). , 656:A160.

Ceccarelli, C., Codella, C., Balucani, N., Bockelée-Morvan, D., Herbst, E., Vastel, C., Caselli, P., Favre, C., Lefloch, B., and Öberg, K. (2022). Organic chemistry in the first phases of solar-type protostars.

Churyumov, K. I., Rozenbush, V. K., Rspayev, F. K., and Gorodetsky, D. I. (1990). Some Results of the Narrow-Band Photometry of Comet Halley (1986 III). , 356:687.

Cochran, A., Barker, E., and Gray, C. (2012). Thirty years of cometary spectroscopy from McDonald observatory. *Icarus*, 218(1):144–168.

Cochran, A. L. (1985). A re-evaluation of the Haser model scale lengths for comets. , 90:2609–2614.

Cochran, A. L. (1987). Another Look at Abundance Correlations Among Comets. , 93:231.

Cochran, A. L., Barker, E. S., Ramseyer, T. F., and Storrs, A. D. (1992). The mcdonald observatory faint comet survey: Gas production in 17 comets. *Icarus*, 98(2):151–162.

Cochran, A. L. and Cochran, W. D. (1990). Observations of CH in comets P/Brorsen-Metcalf and P/Halley. In Huebner, W. F., Wehinger, P. A., Rahe, J., and Konno, I., editors, *Observations of Recent Comets*, pages 22–27.

Cochran, A. L. and Cochran, W. D. (2002). A high spectral resolution atlas of comet 122p/de vico. *Icarus*, 157(2):297–308.

Cochran, A. L. and McKay, A. J. (2018). Strong CO^+ and N_2^+ Emission in Comet C/2016 R2 (Pan-STARRS). , 854(1):L10.

Cochran, A. L. and Schleicher, D. G. (1993). Observational Constraints on the Lifetime of Cometary H_2O. , 105(1):235–253.

Cottin, H. and Fray, N. (2008). Distributed sources in comets. *Space Science Reviews*, 138:179–197.

Cremonese, G., Capria, M. T., and de Sanctis, M. C. (2007). Catalog of the emission lines in the visible spectrum of comet 153P/Ikeya-Zhang. , 461(2):789–792.

De Almeida, A. A., Singh, P. D., and Burgoyne, C. M. (1989). Haser model cn, c2 and c3 production rates in some comets. *Earth, Moon, and Planets*, 47.

de León, J., Licandro, J., de la Fuente Marcos, C., de la Fuente Marcos, R., Lara, L. M., Moreno, F., Pinilla-Alonso, N., Serra-Ricart, M., De Prá, M., Tozzi, G. P., Souza-Feliciano, A. C., Popescu, M., Scarpa, R., Font Serra, J., Geier, S., Lorenzi, V., Harutyunyan, A., and Cabrera-Lavers, A. (2020). Visible and near-infrared observations of interstellar comet 2I/Borisov with the 10.4-m GTC and the 3.6-m TNG telescopes. *Monthly Notices of the Royal Astronomical Society*, 495(2):2053–2062.

Dones, L., Weissman, P. R., Levison, H. F., and Duncan, M. J. (2004). Oort cloud formation and dynamics. In Festou, M. C., Keller, H. U., and Weaver, H. A., editors, *Comets II*, page 153.

Farnham, T. L., Kelley, M. S. P., and Bauer, J. M. (2021). Early activity in comet c/2014 un271 bernardinelli–bernstein as observed by tess. *The Planetary Science Journal*, 2(6):236.

Feldman, P. D., Cochran, A. L., and Combi, M. R. (2004). Spectroscopic investigations of fragment species in the coma. In Festou, M. C., Keller, H. U., and Weaver, H. A., editors, *Comets II*, page 425.

Ferus, M., Kubelík, P., Knížek, A., Pastorek, A., Sutherland, J., and Civiš, S. (2017). High energy radical chemistry formation of hcn-rich atmospheres on early earth. *Scientific Reports*, 7.

Fink, U. (1994). The Trend of Production Rates with Heliocentric Distance for Comet P/Halley. , 423:461.

Fink, U. (2009). A taxonomic survey of comet composition 1985–2004 using ccd spectroscopy. *Icarus*, 201(1):311–334.

Fink, U. and Combi, M. (2004). The effect of using different scale lengths on the production rates of comet 46p/wirtanen. *Planetary and Space Science*, 52(7):573–580.

Fink, U., Combi, M. R., and Disanti, M. A. (1991). Comet P/Halley: Spatial Distributions and Scale Lengths for C 2, CN, NH 2, and H 2O. , 383:356.

Fink, U. and Hicks, M. D. (1996). A survey of 39 comets using CCD spectroscopy. , 459:729–743.

Fornasier, S., Hasselmann, P. H., Barucci, M. A., Feller, C., Besse, S., Leyrat, C., Lara, L., Gutierrez, P. J., Oklay, N., Tubiana, C., Scholten, F., Sierks, H., Barbieri, C., Lamy, P. L., Rodrigo, R., Koschny, D., Rickman, H., Keller, H. U., Agarwal, J., A'Hearn, M. F., Bertaux, J.-L., Bertini, I., Cremonese, G., Deppo, V. D., Davidsson, B., Debei, S., Cecco, M. D., Fulle, M., Groussin, O., Güttler, C., Hviid, S. F., Ip, W., Jorda, L., Knollenberg, J., Kovacs, G., Kramm, R., Kührt, E., Küppers, M., Forgia, F. L., Lazzarin, M., Moreno, J. J. L., Marzari, F., Matz, K.-D., Michalik, H., Moreno, F., Mottola, S., Naletto, G., Pajola, M., Pommerol, A., Preusker, F., Shi, X., Snodgrass, C., Thomas, N., and Vincent, J.-B. (2015). Spectrophotometric properties of the nucleus of comet 67p/churyumov-gerasimenko from the OSIRIS instrument onboard the ROSETTA spacecraft. *Astronomy &amp Astrophysics*, 583:A30.

Fray, N., Bénilan, Y., Cottin, H., Gazeau, M.-C., Minard, R. D., and Raulin, F. (2004). Experimental study of the degradation of polymers: Application to the origin of extended sources in cometary atmospheres. *Meteoritics & Planetary Science*, 39.

Fulle, M., Colangeli, L., Agarwal, J., Aronica, A., Della Corte, V., Esposito, F., Grün, E., Ishiguro, M., Ligustri, R., Lopez Moreno, J. J., Mazzotta Epifani, E., Milani, G., Moreno, F., Palumbo, P., Rodríguez Gómez, J., and Rotundi, A. (2010). Comet 67P/Churyumov-Gerasimenko: the GIADA dust environment model of the Rosetta mission target. , 522:A63.

Gilbert, A. M., Wiegert, P. A., Unda-Sanzana, E., and Vaduvescu, O. (2010). Spectroscopic observations of new Oort cloud comet 2006 VZ13 and four other comets. , 401(4):2399–2405.

Gronkowski, P. and Wesołowski, M. (2015). A model of cometary outbursts: a new simple approach to the classical question. *Monthly Notices of the Royal Astronomical Society*, 451(3):3068–3077.

Haser, L. (1957). Distribution d'intensité dans la tête d'une comète. *Bulletin de la Societe Royale des Sciences de Liege*, 43:740–750.

Helbert, J. (2003). *PhD Thesis*. PhD thesis, Freie Universtat Berlin.

Hills, J. G. (1981). Comet showers and the steady-state infall of comets from the oort cloud. *The Astronomical Journal*, 86:1730–1740.

Hughes, D. W. (1975). Cometary Outbursts, A Brief Survey. , 16:410.

Hui, M.-T., Farnocchia, D., and Micheli, M. (2019). C/2010 u3 (boattini): A bizarre comet active at record heliocentric distance. *The Astronomical Journal*, 157(4):162.

Hyland, M. G., Fitzsimmons, A., and Snodgrass, C. (2019). Near-UV and optical spectroscopy of comets using the ISIS spectrograph on the WHT. *Monthly Notices of the Royal Astronomical Society*, 484(1):1347–1358.

Ipatov, S. I. and A'Hearn, M. F. (2010). Deep Impact ejection from Comet 9P/Tempel 1 as a triggered outburst. In Fernandez, J. A., Lazzaro, D., Prialnik, D., and Schulz, R., editors, *Icy Bodies of the Solar System*, volume 263, pages 317–321.

Ishii, H. and Tamura, S. (1979). The CN Violet (0, 0) Spectrum of Comet 1973 XII Kohoutek. , 31:597–606.

Ivanova, O., Luk'yanyk, I., Tomko, D., and Moiseev, A. (2021). Photometry and long-slit spectroscopy of the split comet C/2019 Y4 (ATLAS). , 507(4):5376–5389.

Ivanova, O., Picazzio, E., Luk'yanyk, I., Cavichia, O., and Andrievsky, S. (2018). Spectroscopic observations of the comet 29p/schwassmann-wachmann 1 at the soar telescope. *Planetary and Space Science*, 157.

Jehin, E., Donckt, M. V., Hmiddouch, S., and Manfroid, J. (2023a). TRAPPIST bright comets production rates: 62P/Tsuchinshan 1, 103P/Hartley, C/2023 H2 (Lemmon), and the 14 November huge outburst of 12P/Pons-Brooks. *The Astronomer's Telegram*, 16338:1.

Jehin, E., Donckt, M. V., Hmiddouch, S., Manfroid, J., Hutsemekers, H., and Moulane, Y. (2022a). TRAPPIST comets production rates: C/2017 K2 (PanSTARR), C/2022 E3 (ZTF), C/2022 P1 (NEOWISE), and 73P/SW-3. *The Astronomer's Telegram*, 15591:1.

Jehin, E., Moulane, Y., Manfroid, J., Donckt, M. V., Pozuelos, F., Ferrais, M., and Hutsemekers, D. (2022b). TRAPPIST comet production rates: 19P/Borrelly, 67P/C-G, 104P/Kowal 2, C/2019 L3 (ATLAS), and C/2021 A1 (Leonard). *The Astronomer's Telegram*, 15186:1.

Jehin, E., Moulane, Y., Manfroid, J., Pozuelos, F., and Hutsemekers, D. (2020). TRAPPIST comet production rates: 88/Howell, C/2020 M3 (ATLAS), C/2020 S3 (Erasmus), 156P/Russell-LINEAR. *The Astronomer's Telegram*, 14101:1.

Jehin, E., Vander Donckt, M., Hmiddouch, S., Manfroid, J., Jabiri, A., and Benkhaldoun, Z. (2023b). TRAPPIST bright comets production rates: 103P/Hartley, 2P/Encke, C/2023 E1 (AT-LAS), C/2020 V2 (ZTF), C/2022 A2 (PANSTARRS), and C/2017 K2 (PANSTARRS). *The Astronomer's Telegram*, 16275:1.

Jewitt, D., Hui, M.-T., Mutchler, M., Weaver, H., Li, J., and Agarwal, J. (2017). A Comet Active Beyond the Crystallization Zone. , 847(2):L19.

Jorda, L., Gaskell, R., Capanna, C., Hviid, S., Lamy, P., Ďurech, J., Faury, G., Groussin, O., Gutiérrez, P., Jackman, C., Keihm, S., Keller, H., Knollenberg, J., Kührt, E., Marchi, S., Mottola, S., Palmer, E., Schloerb, F., Sierks, H., Vincent, J.-B., A'Hearn, M., Barbieri, C., Rodrigo, R., Koschny, D., Rickman, H., Barucci, M., Bertaux, J., Bertini, I., Cremonese, G., Da Deppo, V., Davidsson, B., Debei, S., De Cecco, M., Fornasier, S., Fulle, M., Güttler, C., Ip, W.-H., Kramm, J., Küppers, M., Lara, L., Lazzarin, M., Lopez Moreno, J., Marzari, F., Naletto, G., Oklay, N., Thomas, N., Tubiana, C., and Wenzel, K.-P. (2016). The global shape, density and rotation of comet 67p/churyumov-gerasimenko from preperihelion rosetta/osiris observations. *Icarus*, 277:257–278.

Knight, M. M. and Schleicher, D. G. (2015). Observations of Comet ISON (C/2012 S1) from Lowell Observatory. , 149(1):19.

Korsun, P. P., Kulyk, I. V., Moiseev, A. V., and Afanasiev, V. L. (2012). Comet C/2010X1 (Elenin). Unrealized expectations. *Astrophysical Bulletin*, 67.

Kwon, Y. G., Opitom, C., and Lippi, M. (2023). Coma environment of comet C/2017 K2 around the water ice sublimation boundary observed with VLT/MUSE. , 674:A206.

Lamy, P., Tóth, I. P., Fernández, Y. R., and Weaver, H. (2004). The sizes, shapes, albedos, and colors of cometary nuclei.

Langland-Shula, L. E. and Smith, G. H. (2011). Comet classification with new methods for gas and dust spectroscopy. *Icarus*, 213(1):280–322.

Licandro, J., Popescu, M., de León, J., Morate, D., Vaduvescu, O., De Prá, M., and Ali-Laoga, Victor (2018). The visible and near-infrared spectra of asteroids in cometary orbits. *A&A*, 618:A170.

Massironi, M., Simioni, E., Marzari, F., Cremonese, G., Giacomini, L., Pajola, M., Jorda, L., Naletto, G., Lowry, S., El-Maarry, M. R., Preusker, F., Scholten, F., Sierks, H., Barbieri, C., Lamy, P., Rodrigo, R., Koschny, D., Rickman, H., Keller, H. U., A'Hearn, M. F., Agarwal, J., Auger, A.-T., Barucci, M. A., Bertaux, J.-L., Bertini, I., Besse, S., Bodewits, D., Capanna, C., Da Deppo, V., Davidsson, B., Debei, S., De Cecco, M., Ferri, F., Fornasier, S., Fulle, M., Gaskell, R., Groussin, O., Gutiérrez, P. J., Güttler, C., Hviid, S. F., Ip, W.-H., Knollenberg, J., Kovacs, G., Kramm, R., Kührt, E., Küppers, M., La Forgia, F., Lara, L. M., Lazzarin, M., Lin, Z.-Y., Lopez Moreno, J. J., Magrin, S., Michalik, H., Mottola, S., Oklay, N., Pommerol, A., Thomas, N., Tubiana, C., and Vincent, J.-B. (2015). Two independent and primitive envelopes of the bilobate nucleus of comet 67p. *Nature*, 526(7573):402—405.

Meech, K. J., Kleyna, J. T., Hainaut, O., Micheli, M., Bauer, J., Denneau, L., Keane, J. V., Stephens, H., Jedicke, R., Wainscoat, R., Weryk, R., Flewelling, H., Schunová-Lilly, E., Magnier, E., and Chambers, K. C. (2017). Co-driven activity in comet c/2017 k2 (panstarrs). *The Astrophysical Journal Letters*, 849(1):L8.

Moulane, Y., Benkhaldoun, Z., Jehin, E., Opitom, C., Gillon, M., and Daassou, A. (2017). Monitoring of comets activity and composition with the trappist-north telescope. *Journal of Physics: Conference Series*, 869(1):012079.

Moulane, Y., Jehin, E., Manfroid, J., Hutsemé kers, D., Opitom, C., Shinnaka, Y., Bodewits, D., Benkhaldoun, Z., Jabiri, A., Hmiddouch, S., Donckt, M. V., Pozuelos, F. J., and Yang, B. (2023). Activity and composition of the hyperactive comet 46p/wirtanen during its close approach in 2018. *Astronomy &amp Astrophysics*, 670:A159.

Mumma, M. J. and Charnley, S. B. (2011). The chemical composition of comets—emerging taxonomies and natal heritage. *Annual Review of Astronomy and Astrophysics*, 49(1):471–524.

Munaretto, G., Cambianica, P., Cremonese, G., Fulle, M., Boschin, W., Di Fabrizio, L., Podio, L., and Codella, C. (2023). C/2020 f3 (neowise) production rates from high-resolution tng/harps-n spectra. *Planetary and Space Science*, 230:105664.

Myer, J. A. and Nicholls, R. V. (1970). Resonance Fluorescence of the CN Free Radical. *Nature*, 225:928–929.

Newburn, R. L. and Spinrad, H. (1984). Spectrophotometry of 17 comets. I - The emission features. , 89:289–309.

Opitom, C., Jehin, E., Manfroid, J., Hutsemékers, D., Gillon, M., and Magain, P. (2015a). Five years of comet narrow band photometry and imaging with TRAPPIST. In *AAS/Division for Planetary Sciences Meeting Abstracts #47*, volume 47 of *AAS/Division for Planetary Sciences Meeting Abstracts*, page 506.02.

Opitom, C., Jehin, E., Manfroid, J., Hutsemékers, D., Gillon, M., and Magain, P. (2015b). TRAPPIST photometry and imaging monitoring of comet C/2013 R1 (Lovejoy): Implications for the origin of daughter species. , 584:A121.

Opitom, C., Snodgrass, C., Fitzsimmons, A., Jehin, E., Manfroid, J., Tozzi, G. P., Faggi, S., and Gillon, M. (2017). Ground-based monitoring of comet 67P/Churyumov–Gerasimenko gas activity throughout the Rosetta mission. *Monthly Notices of the Royal Astronomical Society*, 469(Suppl$_2$) : $S222 - -S229$.

Paradowski, M. L. (2020). A new method of determining brightness and size of cometary nuclei. *Monthly Notices of the Royal Astronomical Society*, 492(3):4175–4188.

Randall, C. E., Schleicher, D. G., Ballou, R. G., and Osip, D. J. (1992). Observational Constraints on Molecular Scalelengths and Lifetimes in Comets. In *AAS/Division for Planetary Sciences Meeting Abstracts #24*, volume 24 of *AAS/Division for Planetary Sciences Meeting Abstracts*, page 31.15.

Rickman, H. and Jorda, L. (1998). Comet 46p/wirtanen, the target of the rosetta mission. *Advances in Space Research*, 21(11):1491–1504.

Rosenberg, E. D. and Prialnik, D. (2009). Fully 3-dimensional calculations of dust mantle formation for a model of Comet 67P/Churyumov-Gerasimenko. , 201(2):740–749.

Rubin, M., Fougere, N., Altwegg, K., Combi, M. R., Roy, L. L., Tenishev, V. M., and Thomas, N. (2014). Mass transport around comets and its impact on the seasonal differences in water production rates. *The Astrophysical Journal*, 788(2):168.

Scarmato, T. (2014). Sungrazer Comet C/2012 S1 (ISON): Curve of light, nucleus size, rotation and peculiar structures in the coma and tail. *arXiv e-prints*, page arXiv:1405.3112.

Schleicher, D. G. (2006). Compositional and physical results for rosetta's new target comet 67p/churyumov–gerasimenko from narrowband photometry and imaging. *Icarus*, 181(2):442–457.

Schleicher, D. G. (2010). The fluorescence efficiencies of the cn violet bands in comets. *The Astronomical Journal*, 140(4):973.

Schleicher, D. G. (2022). Comet 21P/Giacobini-Zinner: Narrowband Photometry of the Prototype of Carbon-chain Depleted Comets at Multiple Apparitions. , 3(6):143.

Sierks, H., Barbieri, C., Lamy, P. L., Rodrigo, R., Koschny, D., Rickman, H., Keller, H. U., Agarwal, J., A'Hearn, M. F., Angrilli, F., Auger, A.-T., Barucci, M. A., Bertaux, J.-L., Bertini, I., Besse, S., Bodewits, D., Capanna, C., Cremonese, G., Deppo, V. D., Davidsson, B., Debei, S., Cecco, M. D., Ferri, F., Fornasier, S., Fulle, M., Gaskell, R., Giacomini, L., Groussin, O., Gutierrez-Marques, P., Gutiérrez, P. J., Güttler, C., Hoekzema, N., Hviid, S. F., Ip, W.-H., Jorda, L., Knollenberg, J., Kovacs, G., Kramm, J. R., Kührt, E., Küppers, M., Forgia, F. L., Lara, L. M., Lazzarin, M., Leyrat, C., Moreno, J. J. L., Magrin, S., Marchi, S., Marzari, F., Massironi, M., Michalik, H., Moissl, R., Mottola, S., Naletto, G., Oklay, N., Pajola, M., Pertile, M., Preusker, F., Sabau, L., Scholten, F., Snodgrass, C., Thomas, N., Tubiana, C., Vincent, J.-B., Wenzel, K.-P., Zaccariotto, M., and Pätzold, M. (2015). On the nucleus structure and activity of comet 67p/churyumov-gerasimenko. *Science*, 347(6220):aaa1044.

Swings, P. (1941). Complex structure of cometary bands tentatively ascribed to the contour of the solar spectrum. *Lick Observatory Bulletin*, 508:131–136.

Tancredi, G., Fernández, J. A., Rickman, H., and Licandro, J. (2006). Nuclear magnitudes and the size distribution of jupiter family comets. *Icarus*, 182(2):527–549. Results from the Mars Express ASPERA-3 Investigation.

Usher, H., Miles, R., Redondo, J. M. P., Wooding, B., Kelley, M. S. P., Lister, T., Garcia, F., Buczynski, D., Hale, A., de Oliveira Souza, M., Simpson, E., Eleftheriou, M., Angel, T., Vannini, J., Stoddard-Jones, C., Malaric, M., Rojas, G., Matei, V., Roche, P., students, t., Snodgrass, C., Comet Chasers Project, Faulkes Telescope Project, and LCO Outbursting Objects Key Project (2023). Large Outburst Comet 12P/Pons-Brooks. *The Astronomer's Telegram*, 16270:1.

van Dishoeck, E. F., Bergin, E. A., Lis, D. C., and Lunine, J. I. (2014). Water: From Clouds to Planets. In Beuther, H., Klessen, R. S., Dullemond, C. P., and Henning, T., editors, *Protostars and Planets VI*, pages 835–858.

Venkataramani, K., Ghetiya, S., Ganesh, S., Joshi, U. C., Agnihotri, V. K., and Baliyan, K. S. (2016). Optical Spectroscopy of Comet C/2014 Q2 (Lovejoy) from MIRO. *arXiv e-prints*, page arXiv:1607.06682.

Weaver, H. A., Stern, S. A., and Parker, J. W. (2003). Hubble space telescope stis observations of comet 19p/borrelly during the deep space 1 encounter. *The Astronomical Journal*, 126(1):444.

Wesołowski, M., Gronkowski, P., and Tralle, I. (2020a). Outbursts of comets at large heliocentric distances: Concise review and numerical simulations of brightness jumps. *Planetary and Space Science*, 184:104867.

Wesołowski, M., Gronkowski, P., and Tralle, I. (2020b). Outbursts of comets at large heliocentric distances: Concise review and numerical simulations of brightness jumps. *Planetary and Space Science*, 184:104867.

Ye, Q., Farnham, T. L., Knight, M. M., Holt, C. E., and Feaga, L. M. (2020). Recovery of returning halley-type comet 12p/pons-brooks with the lowell discovery telescope. *Research Notes of the AAS*, 4(7):101.

Yelle, R. V., Soderblom, L. A., and Jokipii, J. R. (2004). Formation of jets in Comet 19P/Borrelly by subsurface geysers. , 167(1):30–36.

Y.Moulane, Jehin, E., Rousselot, P., Manfroid, J., Shinnaka, Y., Pozuelos, F. J., Hutsemékers, D., Opitom, C., Yang, B., and Benkhaldoun, Z. (2020). Photometry and high-resolution spectroscopy of comet 21p/giacobini-zinner during its 2018 apparition. *Astronomy &amp Astrophysics*, 640:A54.

Zucconi, J. M. and Festou, M. C. (1985). The fluorescence spectrum of the CN radical in comets. , 150(2):180–191.